Paleoceanography and Paleoclimatology

RESEARCH ARTICLE
10.1029/2023PA004745

Key Points:
- Penghu Canyon levee sediments have been derived from southwest Taiwan rivers since last deglaciation
- East Asian summer monsoon and typhoons control the chemical weathering intensity and soil erosion of southwest Taiwan river basins
- Sediment to Taiwan margin is less chemically weathered during the middle and late Holocene due to short residence time induced by typhoons

Supporting Information:
Supporting Information may be found in the online version of this article.

Correspondence to:
Z. Liu and C. Colin,
lzhifei@tongji.edu.cn;
christophe.colin@universite-paris-saclay.fr

Citation:
Bertaz, J., Liu, Z., Colin, C., Dapoigny, A., Lin, A. T.-S., Li, Y., & Jian, Z. (2024). Climatic and environmental impacts on the sedimentation of the SW Taiwan margin since the last deglaciation: Geochemical and mineralogical investigations. *Paleoceanography and Paleoclimatology*, *39*, e2023PA004745. https://doi.org/10.1029/2023PA004745

Received 15 AUG 2023
Accepted 2 JUL 2024

Author Contributions:
Conceptualization: Zhifei Liu, Christophe Colin
Formal analysis: Joffrey Bertaz, Yanli Li
Funding acquisition: Zhifei Liu, Christophe Colin
Investigation: Joffrey Bertaz, Zhifei Liu, Christophe Colin, Andrew Tien-Shun Lin, Yanli Li, Zhimin Jian
Methodology: Joffrey Bertaz, Zhifei Liu, Christophe Colin, Arnaud Dapoigny
Supervision: Zhifei Liu, Christophe Colin
Writing – original draft: Joffrey Bertaz
Writing – review & editing: Joffrey Bertaz, Zhifei Liu, Christophe Colin, Arnaud Dapoigny, Andrew Tien-Shun Lin, Zhimin Jian

Climatic and Environmental Impacts on the Sedimentation of the SW Taiwan Margin Since the Last Deglaciation: Geochemical and Mineralogical Investigations

Joffrey Bertaz[1,2], Zhifei Liu[1], Christophe Colin[2], Arnaud Dapoigny[3], Andrew Tien-Shun Lin[4], Yanli Li[1], and Zhimin Jian[1]

[1]State Key Laboratory of Marine Geology, Tongji University, Shanghai, China, [2]Université Paris-Saclay, CNRS, GEOPS, Orsay, France, [3]Laboratoire des Sciences du Climat et de l'Environnement, LSCE/IPSL, CEA CNRS-UVSQ, Université Paris-Saclay, Gif-sur-Yvette, France, [4]Department of Earth Sciences, National Central University, Taoyuan, Taiwan

Abstract Many scientific studies have been conducted to constrain present and past source-to-sink processes and their controlling factors. The role of typhoon and monsoon rainfall on chemical weathering and soils erosion in east Asia is still not well established. Clay minerals and major elements, combined with Nd and Sr isotopic compositions were analyzed on sediments from Core MD18-3569 located on the Taiwan margin in the northeastern South China Sea. The aim was to reconstruct the weathering history of small river basins of southwest Taiwan and to establish the impact of East Asian summer monsoon and typhoon rainfall on source to sink processes since the last glacial period. $^{87}Sr/^{86}Sr$ and εNd values and predominant illite-chlorite indicate that the rivers of southwest Taiwan is the sole source of sediments to Core MD18-3569 since last deglaciation. Variations in clay mineral assemblages and major elements allowed us to evaluate the intensity of past weathering in the rivers of southwest Taiwan. We demonstrated that long-term changes of chemical weathering intensity record from Taiwan are driven by changes in the summer monsoon rainfall. The deglaciation is characterized by a progressive increase in the intensity of chemical weathering, which peaked at the beginning of the Holocene. The chemical weathering degree of sediments from Taiwan decreases during the Holocene concurrently with a weakening of the summer monsoon, increase in typhoon activity, and changes in the vegetation cover. All these processes induce soil erosion, regressive pedogenesis, due to shorter residence time of minerals in the soils of southwest Taiwan.

Plain Language Summary East Asian summer monsoon and typhoon rainfall are important controls on the sediment transfer from land-sea. It is important to understand their impacts on chemical weathering and soil erosion. We analyzed the clay mineralogy and geochemistry of sediments from Core MD18-3569, from the Taiwan margin in the South China Sea, to trace the provenance of the sediments and reconstruct the chemical weathering history of soils of southwestern Taiwan since last glacial period. Clay minerals and Nd and Sr isotopic compositions determine that the rivers of southwest Taiwan are the sources of sediments to Core MD18-3569. Changes in chemical weathering intensity from Taiwan, recorded by clay mineral assemblages and major elements, are controlled by the East Asian summer monsoon precipitation and temperature changes from the last glacial period to the early Holocene. Chemical weathering intensity in southwestern Taiwan reaches its maximum in the early Holocene, which is associated with the increase in monsoon precipitation and temperature. During the Holocene, the weakening of the summer monsoon rainfall is accompanied by changes in vegetation cover and an increase extreme typhoon rainfall, resulting in significant soil erosion, shortening of sediment residence time, and reducing chemical weathering intensity in the southwestern of Taiwan.

1. Introduction

Taiwan Island is characterized by one of the highest rates of tectonic uplift in the world (up to ~20 mm/yr, Ching et al., 2011) and is under the East Asian summer monsoon (EASM) and typhoon-driven precipitation regimes. This contributes to the transfer of large amounts of sediment directly to the East Asian marginal seas through several submarine canyons (e.g., the Gaoping and Penghu Canyons). EASM is a regional feature of the global monsoon system, the global long-term variations are controlled by solar radiation and precession (An et al., 2015; Braconnot et al., 2008; Wang et al., 2017). The regional monsoons respond to regional forcings and have diverse behaviors at shorter timescales. Because of East Asia land-sea configuration (Tibetan Plateau, Indian and Pacific Oceans), the EASM is considered the strongest and largest monsoon system (An et al., 2015). Marine sediments collected on the East Asian margins, therefore, constitute an ideal archive for investigating the intensity of past chemical and physical weathering through time at a high temporal resolution and with respect to various local, regional and global forcings (e.g., climatic, anthropic).

During the late Quaternary, changes in EASM rainfall and typhoon frequency (Clift, 2020; Ding et al., 2016; Selvaraj et al., 2007; Y. Zhang et al., 2018) could have resulted in variations in the sediment budget delivered by a number of rivers to the northeastern South China Sea (SCS) from South China, Taiwan, and Luzon (Clift & Sun, 2006; Hu et al., 2020; Lei et al., 2015; Moy et al., 2002; Wang et al., 2015; Y. Zhang et al., 2018; Zhao et al., 2018). On orbital timescales, paleoclimatic reconstructions suggest that temporal intervals characterized by a reinforcement of EASM rainfall are associated with an increase in soil alteration, runoff, and transfer of sediments from large Asian rivers to the ocean (Boulay et al., 2005; Colin et al., 2010; Gebregiorgis et al., 2016; Liu et al., 2016; Xue et al., 2005). Such climatic variations are associated with changes in the sources and transportation of sediments delivered to the SCS (Liu et al., 2016) and are recorded by variations in clay mineral assemblages and geochemistry of the sediments deposited in the SCS (e.g., Boulay et al., 2005; Colin et al., 2010; Liu et al., 2016).

Several forcings (such as climate, tectonics, and lithology) control the morphology of Taiwan. Taiwan has been characterized by rapid and irregular uplift over time since the late Miocene (Huang et al., 1997). Intervals of high uplift induce a steeper river slope, which leads to stronger physical erosion induced by the enhanced power of rivers to incise bedrocks (Bull, 1990; Hsieh & Knuepfer, 2001, 2002). Climatic conditions of Taiwan with heavy rains play a key role in the weathering and morphological changes of Taiwan river basins (Hsieh & Knuepfer, 2001, 2002; Molnar, 2001). Enhanced hydrolysis conditions associated with rainfall conditions can induce rapid leaching of the most labile elements. This phenomenon is also enhanced by the breaking up of rocks by erosion, leading to greater surface alteration (Rasmusson & Carpenter, 1982). Thus, in a tectonically active region with marked climatic variability, weathering is triggered by the variation of the interactions between these forcings and their effects on erosion (Riebe et al., 2001).

Previous studies of terrigenous fractions from cores collected in the SCS have indicated a strong link between sea-level variation, monsoon rainfall, and geochemical and mineralogical variations on different time scales, for example, million-year (Boulay et al., 2007; Yu et al., 2016), orbital (Boulay et al., 2005; Colin et al., 2010; Liu et al., 2016), and millennial scales (Zhao et al., 2018). All these results suggest that the supply of sediments by Asian rivers and the hydrology of the SCS were strongly reactive to past changes in monsoon rainfall and sea-level.

However, consensus has yet been reached regarding the relationship between precipitation and chemical weathering. Several previous studies have shown that enhanced degree of silicate chemical weathering occurred in large river basins during warm, humid periods of the late Quaternary (Chen et al., 2016; Miriyala et al., 2017; Sang et al., 2022). In contrast, an intensification of monsoon rainfall has also been linked to a reduction in the residence time of sediments in river basins, like those of Taiwan, and thus to a weakening of chemical weathering (Bi et al., 2015; Dosseto et al., 2010; Dou et al., 2016; Zhao et al., 2017). In recent years, much attention has focused on chemical weathering and erosion of soils and rocks in tropical regions and their link to climatic and environmental changes or human activities; this is because understanding soils and "critical zones" are pressing issues for our societies (Adhikari & Hartemink, 2016; Brantley et al., 2007; Latour, 2014). Present-day changes have been studied with the development of monitoring observatories (Brantley et al., 2017; Gaillardet et al., 2018). Such results demonstrated that the paleo-soils of small mountain rivers, comparable to the SW Taiwan river system, are strongly controlled by climatic and tectonic changes (Arnaud et al., 2012; Bajard et al., 2016; Bajard, Poulenard, Sabatier, Develle, et al., 2017, Bajard, Poulenard, Sabatier, Etienne, et al., 2017; Sun & Colin, 2014) and by human activities (Sabatier et al., 2014). The history of the state of pedogenesis in critical zones can be deduced from clay mineralogical, geochemical, and palynological variations in sedimentary records such as those from lakes or watersheds. The formation of soils during progressive pedogenesis results in the leaching of more mobile elements and influences the production of clay minerals. The vegetation of small river basins is also very sensitive to the level of soil maturity and pedogenesis; weathered soils are favorable for the installation of stable cover such as forests and trees (Bajard et al., 2016; Sun & Colin, 2014). Inversely, during regressive pedogenesis the erosion of soil leads to the production of illite (Sun & Colin, 2014), the transfer of mobile element-enriched sediments (Arnaud et al., 2012; Bajard, Poulenard, Sabatier, Develle, et al., 2017, Bajard, Poulenard, Sabatier, Etienne, et al., 2017), and the replacement of trees by herbs (Bajard et al., 2016; Sun & Colin, 2014).

Deep-sea sediments from the southwestern margin of Taiwan have great potential for reconstructing a continuous record of past weathering of SW Taiwan since the last glacial period associated with regional and global forcings. SW Taiwan has a particular land-sea configuration, with a narrow shelf and numerous submarine canyons, such as the Gaoping and Penghu Canyons (Figure 1), which facilitate the rapid transport of sediments from Taiwan rivers to the deep-basin via rbidity currents (Liu et al., 2008; Milliman & Syvitski, 1992; Y. Zhang et al., 2018). The Gaoping Canyon is connected to the Gaoping River mouth and sediments are transported directly by hyperpycnal and turbidity flows that are strongly dependent on typhoon events (~70%) and, to a lesser extent, on earthquakes in the region (Liu et al., 2016; Y. Zhang et al., 2018). At the present time, the Penghu Canyon is not directly connected to any river mouth but might have been connected, through the Penghu Channel, to SW Taiwan rivers during glacial low sea level intervals. Sediments transported by these canyons have been partially redistributed along the SW Taiwan margin by Pacific Deep Water (PDW) currents, which enter the SCS through the Luzon Strait.

In this study, we conduct high-resolution analyses of clay mineral and major element concentrations, as well as Sr and Nd isotopic measurements, of a core located on the eastern bank of the Penghu Canyon; our aim is to reconstruct (i) temporal variations in sediment sources and transfer to the northeastern SCS and (b) changes in the weathering degree of SW Taiwan and their potential links to climatic changes since the last glacial period.

2. Climatic and Geological Settings

2.1. East Asian Monsoon and SCS Hydrology

The East Asian monsoon is characterized by a seasonal reversal of wind direction and latitudinal shift of the intertropical convergence zone (ITCZ) associated with intense humidity over the northern SCS (Ruddiman, 2001; Webster, 1994, 1998) (Figure 1). In summer, the ITCZ is located between 20 and 35°N, in the SCS region, the EASM is responsible for 80% of the regional yearly precipitation. In contrast, in winter, the ITCZ shifts southwards to between 0 and 20°S (Wang et al., 2003). The precipitation rates are about 2,500 mm/yr on Taiwan, 1,700–2,000 mm/yr in South China, and 1,900–2,100 mm/yr on Luzon (Dadson et al., 2003; Liu et al., 2007, 2009). Taiwan rivers, the Pearl River, and Luzon rivers supply 176 Mt/yr, 102 Mt/yr, and 13 Mt/yr of detrital sediments to the northeastern SCS, respectively (Dadson et al., 2003; Liu et al., 2009; Zhang et al., 2012). The monsoon winds and the Kuroshio intrusion control the seasonal reversal of the surface ocean circulation pattern of the northeastern SCS (Hu et al., 2000).

The Luzon Strait, with a water depth of about 2,400 m, is the only deep-sea channel connecting the SCS to the western Pacific Ocean (L. Li & Qu, 2006; Qu et al., 2006). At the surface, the intrusion of the Kuroshio Current into the northern SCS occurs through the Luzon Strait, from which it flows along the margin of Taiwan in the northern SCS (Caruso et al., 2006). During the winter, the dominant southwestward winds drive the formation of surface cyclonic gyres in the SCS and the coastal current flowing northwards on the South China shelf (Fang et al., 1998; Wu, 2014). During the summer, the dominant northeastward winds induce an anti-cyclonic surface gyre and a surface coastal current which flows northwards (Fang et al., 1998; Wu, 2014).

A vertical sandwich structure has been recognized in the Luzon Strait, where the inflow of surface and deep waters to the SCS is compensated by the outflow of intermediate water mass to the Pacific Ocean (Gan et al., 2016; Tian et al., 2006; Yuan, 2002; Zhu et al., 2019). Recent studies indicate that the exchange of intermediate water (from 500 to 1500 m) between the SCS and the Pacific Ocean is very complex with strong seasonal variability. During the summer, there is a westward inflow in the northern part of the strait and an eastward outflow in the southern part, while the flow pattern across the strait is reversed in winter (Xie et al., 2011; Yang et al., 2010; Zhu et al., 2019). After entering the SCS through the Luzon Strait, the deep-water current (2,000–2,500 m) turns northwestwards along the southern margin of Taiwan, and then turns southwestwards along the continental margin of South China (Qu et al., 2006; Wang et al., 2011) (Figure 1). This deep-sea circulation corresponds to the SCS Contour Current system that contributes, like the Kuroshio Current at the sub-surface, to the redistribution of vast amounts of sediments along the southern margin of Taiwan (Liu et al., 2016; Zhao et al., 2015).

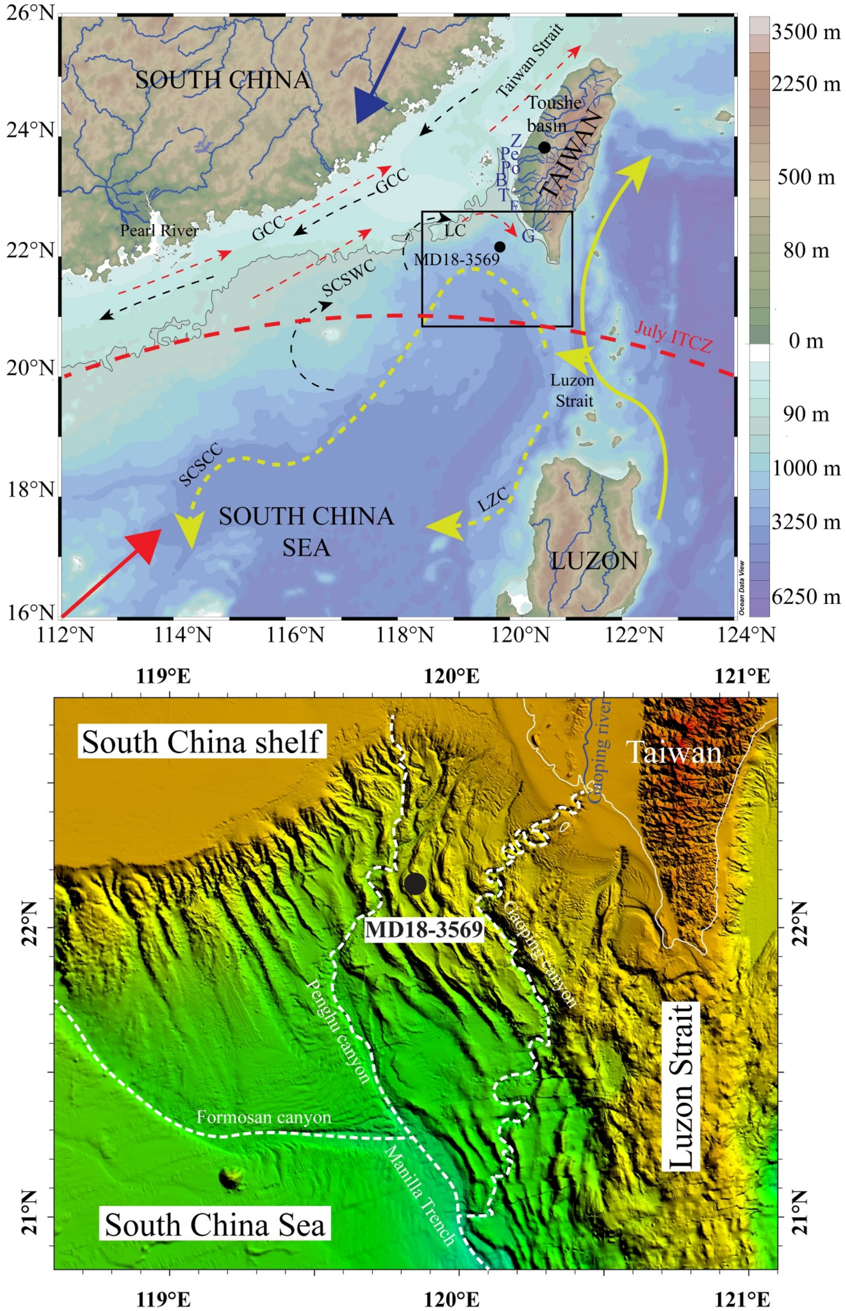

Figure 1. Bathymetric maps of the northeastern SCS showing the location of Core MD18-3569. Location of the Toushe basin discussed in this study is also indicated. Main surface- and deep-current patterns (LZC: Luzon deep current; SCSCC: SCS contour current; SCSWC: SCS warm current; LC: Loop current; GCC: Guangdong coastal current) (Liu et al., 2016), southern limit of July intertropical convergence zone (ITCZ) and winter and summer monsoon wind directions are reported (Wang et al., 2003; Webster, 1994). The SW Taiwan rivers are also reported (Z: Zhuoshui; Pe: Peikang; Po: Potzu; Ba: Bachang; T: Tsengwen; E: Ehrjen; G: Gaoping) The gray line represents the coastline of South China and Taiwan shelves during low sea-level periods.

2.2. Sources of Northeastern SCS Sediments

The river basins of SW Taiwan, Luzon, and South China are the main sources of detrital sediments for the northeastern SCS (Dadson et al., 2003; Liu et al., 2009; Milliman & Farnsworth, 2011; Zhang et al., 2012).

The coastal plain of SW Taiwan consists mainly of Pliocene to Holocene sedimentary formations. The eastern and central mountain ranges are characterized by Miocene and Pliocene sedimentary, metamorphic, and volcanic rocks. Due to a high degree of physical erosion induced by heavy monsoon rainfall and rapid uplift (up to ∼20 mm/yr, Ching et al., 2011), the clay mineral assemblage of sediments delivered by the Taiwan rivers is characterized by dominant proportions of illite (average 56%) and chlorite (average 36%), with minor proportions of kaolinite and smectite (Liu et al., 2010).

South China is a cratonic region composed mainly of Paleozoic and Mesozoic sandstones, mudstones, and limestones with a significant presence of Mesozoic and Cenozoic granitic intrusive rocks. This region is characterized by intensive chemical weathering due to the relatively heavy monsoon precipitation and tectonic stability. Thus, the sediments transported to the northeastern SCS by the Pearl River are mainly composed of kaolinite (46%) and illite (35%), with a smaller proportion of chlorite (18%) and negligible amounts of smectite (1%). Due to the geological and climatic settings, sediments from South China are experiencing higher intensity of chemical weathering than in Taiwan. Chemical weathering intensity affects the chemical and crystallinity features of minerals such as illite (Hu et al., 2014). This is characterized by higher values of illite chemistry index and crystallinity of sediments transported by the Pearl River in comparison to those of sediments from Taiwan (Liu Z et al., 2008, 2010).

In contrast, Luzon consists mainly of volcanic rocks, such as basalts and andesites. Under tropical climatic conditions and strong EASM precipitation, the clay mineral assemblage of the rivers draining this basaltic province differs significantly from sediments from Taiwan and South China with dominant smectite (87%) and low contents of illite (1%), chlorite (7%), and kaolinite (5%) (Liu et al., 2009).

3. Material and Methods

3.1. Material and Age Model

The Calypso Core MD18-3569 (22°09.30'N, 119°49.24'E; 40.08 m in length; 1,320 m water depth) was collected in June 2018 on the eastern bank of the Penghu Canyon during the HYDROSED cruise aboard the R/V *Marion Dufresne* (Figure 1). The lithology of Core MD18-3569 consists mainly of a greenish gray homogenous hemipelagic mud without any visible turbidites. For this study, the upper 15 m of Core MD18-3569 has been investigated with a sampling resolution of 5 cm for the upper 3 m and 8–15 m depth intervals and of 2.5 cm for the 3–8 m depth interval. A total of 381 samples were thus collected. They were used to analyze clay minerals and major elements, and among them, 33 samples were selected for Sr and Nd isotopic measurement of carbonate-free detrital bulk and clay-size (<2 μm) fractions.

The age model of the studied section of Core MD18-3569 was established using linear interpolation between eight calibrated AMS ^{14}C dates obtained from planktonic foraminifer *G. ruber* (250–355 μm) combined with oxygen isotope stratigraphy of planktonic foraminifer *G. ruber* (250–355 μm) (Chen et al., 2021) (Figure S1 in Supporting Information S1). The *G. ruber* δ^{18}O record displays a glacial to Holocene δ^{18}O difference (considering maximum and minimum values) of ∼3.1‰ (Chen et al., 2021) (Figure S1 in Supporting Information S1). The mean sedimentation rate of Core MD18-3569 is high (54.7 cm/Kyr) (Figure S1 in Supporting Information S1). It increases from 34.9 to 52.0 cm/Kyr during the last deglaciation and reaches the maximum value of 72.9 cm/Kyr after 4 cal Kyr BP. This permits us to obtain a high temporal resolution (about 85 years) records of clay mineralogy and geochemistry during the past 32 Kyr.

3.2. Clay Mineralogical Analysis

The clay mineral determination was obtained by X-ray diffraction (XRD) performed on a PANalytical X'Pert PRO diffractometer hosted at the *State Key Laboratory of Marine Geology* (Tongji University). The analytical procedure used has been described in detail by Liu et al. (2004). In brief, after decarbonization (20% acetic acid) and removal of organic matter (H_2O_2), the clay fraction (<2 μm) was extracted following Stokes' Law. The XRD measurements were performed on oriented thin sections that had been successively air dried, saturated with ethylene glycol under vacuum for 24 hr, and heated at 490°C for 2 hr. Semi-quantitative estimates of the peak areas of the basal reflections for the main clay mineral groups (smectite: 15–17 Å; illite: 10 Å; and kaolinite/chlorite: 7 Å) were carried out on the ethylene glycol saturation diffractogram using MacDiff software. Kaolinite and chlorite were distinguished using the 3.57/3.54 Å peak areas. Illite chemistry was calculated using 10 Å/5 Å peak areas and illite crystallinity using the full-width at half-maximum (FMWH) value of the 10 Å peak. Replicate analysis of the sample produced results with a relative error margin of ±2% (2σ).

3.3. Major Element Analysis

Major elements (SiO_2, Al_2O_3, Fe_2O_3, K_2O, CaO, MgO, Na_2O) were analyzed using X-ray fluorescence (XRF) on a PANalytical Axios spectrometer at the *State Key Laboratory of Marine Geology* (Tongji University) on the same samples processed for the mineralogical analyses. Salt was removed after three centrifugations of a solution of deionized water and finely ground samples; supernatant water was removed between the centrifugations. After the salt removal, the samples were dried. Then, 3.5 g of finely ground samples were used to form pellet tablets with boric acid and a press machine. Samples were then analyzed by X-ray fluorescence in an X-ray spectrometer. GSD-15, GSD-16, and GSR-6 standards were used to control the analysis precision every 20 samples and showed an average standard deviation of less than ±2%. Major elements were expressed as their oxides (%) as absolute bulk content of samples. The measurements were not processed on carbonate-free bulk sediments. Calcium oxide (CaO) has been corrected from calcium carbonate with P and Na molar content following Singh et al., 2005; Sang et al., 2018; Jiwarungrueangkul et al., 2019, and the siliciclastic calcium oxide is expressed as CaO*.

3.4. Sr and Nd Isotope Analysis

Sr and Nd isotopic compositions were analyzed on the carbonate-free bulk and clay-size (<2 μm) siliciclastic fractions. The clay fraction was extracted following the same analytical procedure used for XRD measurements. The carbonate-free fractions were analyzed after decarbonation (20% acetic acid) and the removal of organic matter (H_2O_2). Samples were first dissolved in HF-$HClO_4$ and HNO_3-HCl mixtures. Sr and REEs were then separated using a Biorad column packed with AG50WX-8 200–400 mesh cationic exchange resin and using 2 N HCl and 2.5 N HNO_3, respectively. The Sr fraction was then purified on a 20-μl Sr-Spec column consisting of a polyethylene syringe with a 4 mm Ø millex filter (Colin et al., 1999). Nd was purified from the REEs fraction using Ln-Spec resins and following the detailed analytical procedures described in Copard et al. (2010).

Sr and Nd isotopic compositions were measured using a Thermo Scientific Multi-Collector Induced Coupled Plasma Mass Spectrometer (MC-ICP-MS *NEPTUNE^{Plus}*) hosted at the *Laboratoire des Sciences du Climat et de l'Environnement (LSCE)*, Gif-sur-Yvette (France). For the Sr and Nd isotope analyses, sample and standard concentrations were matched at 20 ppb. During the analytical sessions, every group of three samples was bracketed with analyses of appropriate Sr standard solution NIST SRM987 ($^{87}Sr/^{86}Sr$ of 0.710245 ± 0.000016) and Nd standard solution JNdi-1 ($^{143}Nd/^{144}Nd$ of 0.512115 ± 0.000006) (Lugmair et al., 1983; Tanaka et al., 2000). The Sr and Nd isotope ratios were corrected from mass bias according to the exponential law relative to $^{146}Nd/^{144}Nd$ = 0.7219 and $^{86}Sr/^{88}Sr$ = 0.1194. Nd isotopic compositions are expressed as $\varepsilon_{Nd}(0) = [(^{143}Nd/^{144}Nd)_{sample}/(^{143}Nd/^{144}Nd)_{CHUR}-1] \times 10{,}000$, with the present-day $(^{143}Nd/^{144}Nd)_{CHUR}$ of 0.512638 (Jacobsen & Wasserburg, 1980). The analytical errors for each sample analysis were taken as the external reproducibility of the JNdi-1 or NIST SRM987 standards unless the internal error was larger.

4. Results

4.1. Clay Mineralogy

The clay mineral assemblage of Core MD18-3569 is dominated by illite (45%–59%, average 52%) and chlorite (27–39, average 32%), along with a moderate proportion of smectite (4%–22%, average 12%) and a minor proportion of kaolinite (2%–8%, average 4%) (Figure 2). In general, variations in the proportions of illite and chlorite are similar, and they are inversely correlated to those of smectite and, to a lesser extent, to kaolinite distributions (Figure 3).

Smectite content is low (average around 10%–12%) during the late Holocene and in the time interval of 20–12 cal Kyr BP, and slightly higher (average around 14%) during the early Holocene between 11 and 5 cal Kyr BP. Similarly, kaolinite content is slightly higher (4%) during 11–5 cal kyr BP and lower (3%) during the late Holocene and last glacial periods. Illite and chlorite contents present inverse variations to smectite with high proportions during the late Holocene and last glacial period. Illite and chlorite contents are relatively lower during the early Holocene (11 and 5 cal Kyr BP) (Figure 2).

10.1029/2023PA004745

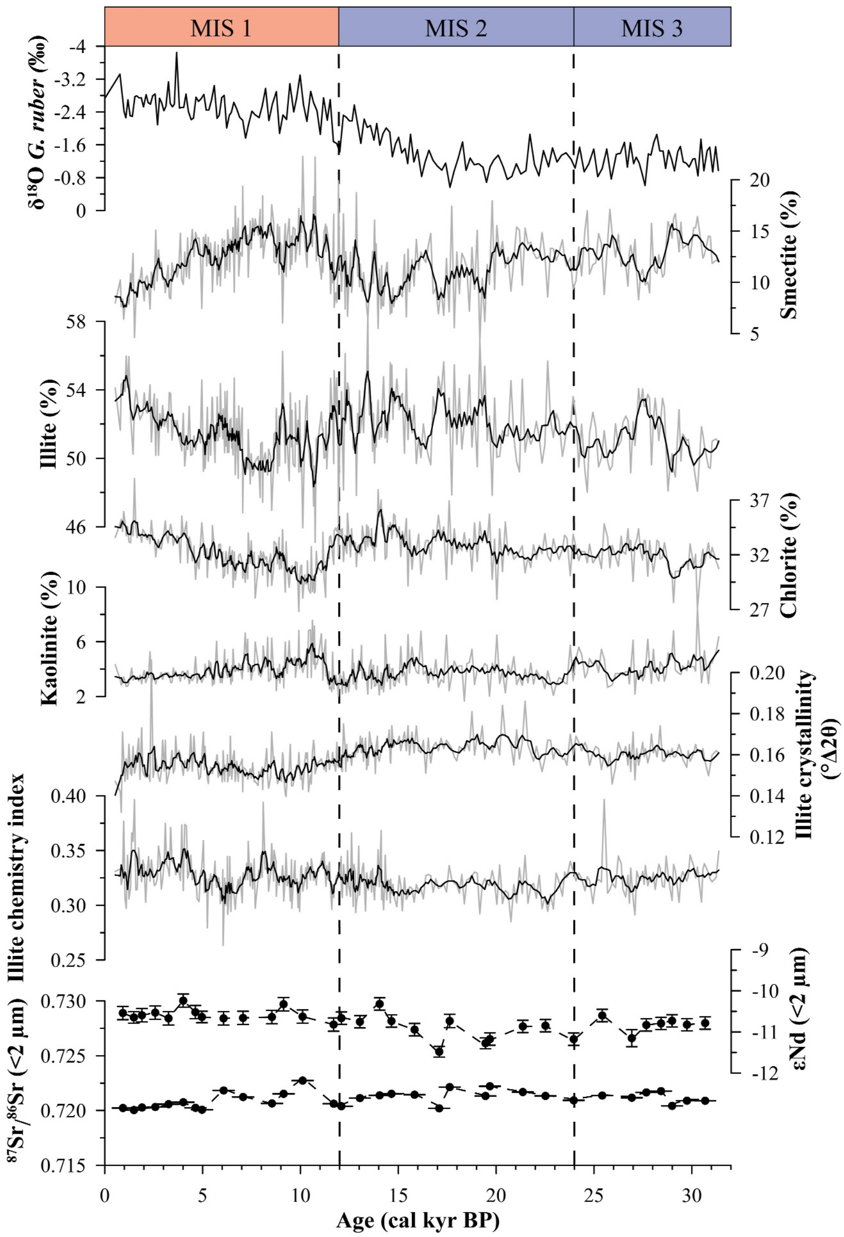

Figure 2. Temporal variations of clay mineral assemblage, illite crystallinity, illite chemistry index, clay fraction (<2 μm) Nd and Sr isotopic compositions, and *G. ruber* $\delta^{18}O$ of Core MD18-3569 during the last 32 Kyr. *G. ruber* $\delta^{18}O$ from Chen et al. (2021).

Illite crystallinity and illite chemistry index vary within narrow ranges of 0.132–0.206° Δ2θ (average 0.158° Δ2θ) and of 0.264–0.397 (average 0.324), respectively. Both mineralogical parameters do not display significant variations over the past 32 Kyr.

4.2. Major Elements

Major elements of Core MD18-3569 sediments mainly include SiO_2 (61.9%–67.5%, average 65%), Al_2O_3 (13.9%–16.6%, average 15%), and Fe_2O_3 (5.3%–7.2%, average 6.2%) with lower concentrations of K_2O (2.8%–3.4%, average 3%), MgO (1.9%–2.4%, average 2.1%), Na_2O (1.1%–1.3%, average 1.2%), and CaO (0.9%–1.2%, average 1%) (Figure 4). Al_2O_3, Fe_2O_3, K_2O, and MgO contents were relatively low and stable in the interval of 32–18 cal kyr BP and then increased progressively at 18 cal Kyr BP to reach a maximum at 10 cal kyr BP.

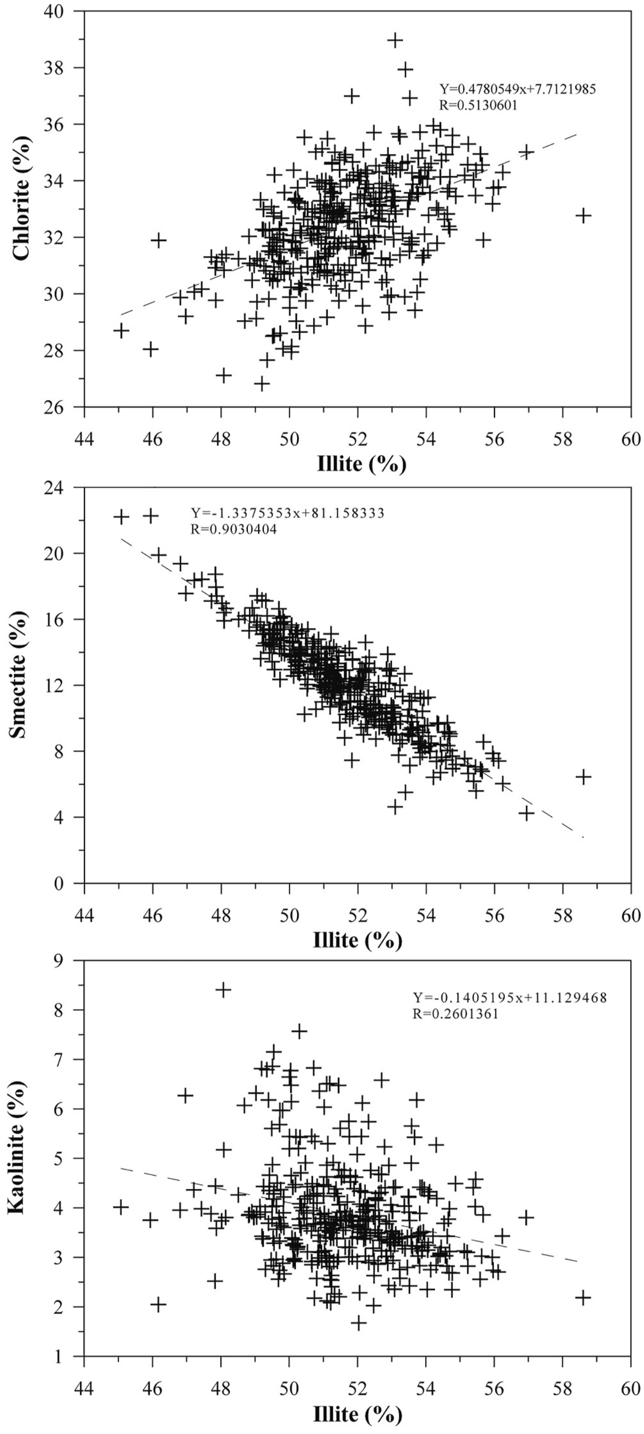

Figure 3. Correlation plots of clay mineral groups of Core MD18-3569. (a) Chlorite (%) versus illite (%). (b) Smectite (%) versus illite (%). (c) Kaolinite (%) versus illite (%).

Thereafter, their concentrations decreased until ~7.8 cal kyr BP and then have increased slightly up to the present time. Long-term variations in SiO_2, Na_2O, and CaO concentrations are inversely correlated to those of Al_2O_3, Fe_2O_3, K_2O, and MgO. SiO_2, Na_2O, and CaO concentrations decreased during the time interval of 20–10 cal kyr BP and increased at ~8.3 cal Kyr BP (Figure 4).

4.3. Sr-Nd Isotopic Compositions

εNd values of bulk siliciclastic sediments display a narrow range from −11.63 ± 0.15 to −10.96 ± 0.13 (Figure 2). εNd values of clay fraction also present a narrow range from −11.48 ± 0.13 to −10.28 ± 0.15 with slightly higher values than those obtained for the bulk siliciclastic sediments (Table 1) (Figure 4). $^{87}Sr/^{86}Sr$ ratios of bulk siliciclastic sediments also display a narrow range, from 0.7187 to 0.7213, without any significant variation trends during the past 32 Kyr apart from a peak at 17.1 cal kyr BP (0.7213) (Figure 2). $^{87}Sr/^{86}Sr$ ratios obtained on the clay fraction present slightly higher values (from 0.7197 to 0.7230) from the MIS 3 to the early Holocene (with a maximum centered at 10 cal kyr BP) than the late Holocene, which is associated with a slight decrease of the $^{87}Sr/^{86}Sr$ ratio (Figure 2).

5. Discussions

5.1. Sources of Sediments to the SW Taiwan Margin

Several studies have shown that Sr and Nd isotopic compositions in deep-sea sediments of the northeastern SCS are particularly useful for determining the principal sources of sediments (Boulay et al., 2005; Liu et al., 2005; Wei et al., 2012). Compared to the original bedrock values, εNd values in sediments are usually not significantly influenced by erosion and transportation. In contrast, $^{87}Sr/^{86}Sr$ ratios can be modified significantly within different grain-size fractions because of sorting effects that occur during transport. Several previous studies have shown that the coarse fractions of sediments are characterized by different mineral compositions to the fine fraction. For example, it has been shown that the fine fraction mainly contains clay minerals and micas, which are often characterized by high $^{87}Sr/^{86}Sr$ ratios (Colin et al., 2006; Hu et al., 2012; Innocent et al., 2000; Meyer et al., 2011; Zhao et al., 2017). $^{87}Sr/^{86}Sr$ ratios can be also affected by chemical weathering of Rb-rich minerals such as micas (Colin et al., 2006). Therefore, Sr isotopes can be biased by sorting effects and caution must be considered when constraining sedimentary provenances. Since most previous results for the deep-sea sediments of the SCS and their sedimentary sources have been obtained on the decarbonated bulk sediment or <63 μm fraction, in Figure 5 we have reported the εNd and $^{87}Sr/^{86}Sr$ ratios analyzed on the decarbonated bulk sediments from Core MD18-3569 together with Sr and Nd isotopic compositions of river sediments obtained on the <63 μm fraction.

The narrow ranges of εNd values and $^{87}Sr/^{86}Sr$ ratios of decarbonated bulk sediments (εNd from −11.63 to −10.89 and $^{87}Sr/^{86}Sr$ from 0.7187 to 0.7213) of Core MD18-3569 are similar to those of Taiwan river sediments (εNd from −11.2 to −12.2 and $^{87}Sr/^{86}Sr$ from 0.7176 to 0.7219) (Dou et al., 2016; Liu et al., 2016) (Figure 5). Such Sr and Nd isotopic compositions are in contrast with the εNd and $^{87}Sr/^{86}Sr$ ranges of Luzon river sediments (εNd from +6.4 to +7.4 and $^{87}Sr/^{86}Sr$ from 0.7044 to 0.7052) and Pearl River sediments (εNd from −1.4 to −10.5 and $^{87}Sr/^{86}Sr$ from 0.7275 to 0.7373) (Dou et al., 2016; Goldstein & Jacobsen, 1988; Liu et al., 2016) (Figure 5). More specifically, plots of the εNd and $^{87}Sr/^{86}Sr$ values of the decarbonated sediments of Core MD18-3569 closely overlie the ranges for SW Taiwan rivers (Zhuoshui, Tsengwen, Ehrjen, and Gaoping) (Figure 5). However, variations in

10.1029/2023PA004745

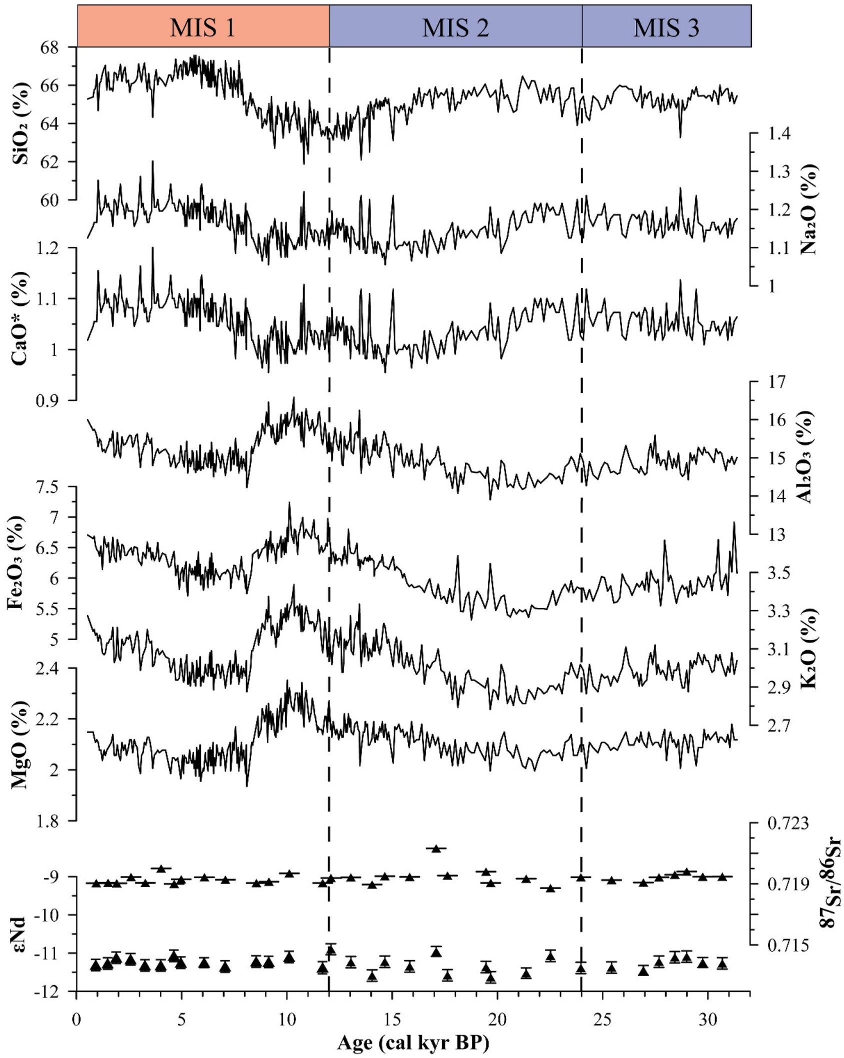

Figure 4. Temporal variations of major element contents (SiO_2, Na_2O, CaO, Al_2O_3, Fe_2O_3, K_2O and MgO) of Core MD18-3569 over the last 32 Kyr. $^{87}Sr/^{86}Sr$ ratio and εNd value of the carbonate-free bulk fractions are also displayed.

the Sr and Nd isotopic compositions of the decarbonated sediments are too small to allow a robust interpretation of changes in the provenance among SW Taiwan rivers since the last glacial period. This implies that the sediment provenance is a mixture of SW Taiwan rivers (Zuoshui: εNd = −12.2, $^{87}Sr/^{86}Sr$ = 0.7192; Tsengwen: εNd = −12.8, $^{87}Sr/^{86}Sr$ = 0.7209; Ehrjen: εNd = −12.6, $^{87}Sr/^{86}Sr$ = 0.7206) (Figure 5).

Nevertheless, such ranges of Sr and Nd isotopic compositions indicate that the main sedimentary source remains as the SW Taiwan river basins and they exclude a significant contribution of sediments deriving from the Luzon rivers as well as the Pearl River (Figure 5). There are slightly higher εNd and $^{87}Sr/^{86}Sr$ ratios for the clay fraction compared to the decarbonated bulk sediments (Table 1) in agreement with previous results obtained in other study areas (Hu et al., 2012; Innocent et al., 2000; Meyer et al., 2011; Zhao et al., 2017). Nevertheless, the narrow ranges of εNd and $^{87}Sr/^{86}Sr$ ratios of the clay-size fraction (<2 μm) confirm that clay mineral sources have remained constant throughout the past 32 Kyr (Figure 6).

Clay mineral assemblage has been used in previous studies to constrain sediment sources and transports to the oceanic margin of the northeastern SCS (Boulay et al., 2005; Liu et al., 2010, 2016; Zhao et al., 2018). Given the contrasted mineralogical signatures of the main sedimentary provinces (e.g., Liu et al., 2016), it is possible to use the clay mineral assemblage of sediments from Core MD18-3569 to better constrain the sources of sediments on the eastern bank of the Penghu Canyon.

Table 1
Sr and Nd Isotopic Compositions Measured on the Carbonate-Free Bulk and Clay-Size (<2 μm) Siliciclastic Fractions of Sediments From Core MD18-3569

Depth (cm)	Age (cal Kyr BP)	$^{87}Sr/^{86}Sr$	±2σ	$^{143}Nd/^{144}Nd$	±2σ	εNd	±2σ
Bulk siliciclastic							
20.5	0.92	0.71904	0.00001	0.512058	0.000008	−11.31	0.15
61.0	1.47	0.71906	0.00001	0.512060	0.000008	−11.27	0.15
91.0	1.89	0.71904	0.00001	0.512068	0.000008	−11.12	0.15
140.5	2.62	0.71944	0.00001	0.512066	0.000008	−11.16	0.15
190.5	3.31	0.71906	0.00001	0.512058	0.000008	−11.32	0.15
241.0	4.04	0.72000	0.00001	0.512058	0.000008	−11.32	0.15
280.5	4.65	0.71899	0.00001	0.512070	0.000008	−11.07	0.15
301.0	4.98	0.71930	0.00001	0.512061	0.000008	−11.25	0.15
370.5	6.13	0.71943	0.00001	0.512061	0.000007	−11.25	0.13
421.0	7.09	0.71927	0.00001	0.512056	0.000008	−11.35	0.15
481.0	8.56	0.71905	0.00001	0.512063	0.000008	−11.22	0.15
511.0	9.16	0.71914	0.00001	0.512062	0.000008	−11.23	0.15
560.5	10.13	0.71968	0.00001	0.512069	0.000008	−11.10	0.15
640.5	11.71	0.71905	0.00001	0.512055	0.000008	−11.38	0.16
661.0	12.13	0.71938	0.00001	0.512079	0.000007	−10.90	0.14
710.5	13.04	0.71942	0.00001	0.512062	0.000008	−11.24	0.15
760.5	14.05	0.71895	0.00001	0.512044	0.000008	−11.59	0.15
790.5	14.65	0.71950	0.00001	0.512062	0.000008	−11.23	0.15
850.5	15.83	0.71945	0.00001	0.512056	0.000008	−11.35	0.15
901.0	17.09	0.72132	0.00001	0.512076	0.000007	−10.96	0.13
920.5	17.63	0.71954	0.00001	0.512044	0.000008	−11.58	0.15
991.0	19.46	0.71979	0.00001	0.512055	0.000008	−11.37	0.15
1000.5	19.68	0.71906	0.00001	0.512042	0.000008	−11.63	0.15
1060.5	21.36	0.71933	0.00001	0.512047	0.000007	−11.52	0.14
1100.5	22.52	0.71872	0.00001	0.512070	0.000008	−11.07	0.15
1150.5	23.96	0.71943	0.00001	0.512054	0.000008	−11.39	0.15
1201.0	25.42	0.71925	0.00001	0.512055	0.000008	−11.38	0.15
1261.0	26.93	0.71908	0.00001	0.512051	0.000007	−11.45	0.13
1300.5	27.67	0.71942	0.00001	0.512063	0.000008	−11.23	0.15
1340.5	28.43	0.71959	0.00001	0.512069	0.000008	−11.11	0.15
1370.5	28.99	0.71980	0.00001	0.512069	0.000008	−11.09	0.15
1411.0	29.75	0.71947	0.00001	0.512062	0.000007	−11.25	0.13
1460.5	30.68	0.71947	0.00001	0.512060	0.000008	−11.27	0.15
Clay size fraction							
20.5	0.92	0.71995	0.00001	0.51210	0.000007	−10.56	0.15
61.0	1.47	0.71972	0.00001	0.512091	0.000008	−10.66	0.13
91.0	1.89	0.72001	0.00001	0.512094	0.000008	−10.61	0.15
140.5	2.62	0.72007	0.00001	0.512097	0.000008	−10.55	0.15
190.5	3.31	0.72039	0.00001	0.512090	0.000008	−10.68	0.15
241.0	4.04	0.72060	0.00001	0.512111	0.000008	−10.28	0.15

Table 1
Continued

Depth (cm)	Age (cal Kyr BP)	$^{87}Sr/^{86}Sr$	±2σ	$^{143}Nd/^{144}Nd$	±2σ	εNd	±2σ
280.5	4.65	0.71997	0.00001	0.512198	0.000008	−10.54	0.15
301.0	4.98	0.71975	0.00001	0.512092	0.000007	−10.65	0.13
370.5	6.13	0.72193	0.00001	0.512091	0.000008	−10.68	0.15
421.0	7.09	0.72120	0.00001	0.512091	0.000008	−10.67	0.15
481.0	8.56	0.72047	0.00001	0.512092	0.000008	−10.65	0.15
511.0	9.16	0.72155	0.00001	0.512107	0.000008	−10.36	0.15
560.5	10.13	0.72305	0.00001	0.512093	0.000008	−10.64	0.15
640.5	11.71	0.72044	0.00001	0.512083	0.000008	−10.82	0.15
661.0	12.13	0.72039	0.00001	0.512091	0.000008	−10.66	0.15
710.5	13.04	0.72113	0.00001	0.512087	0.000008	−10.75	0.15
760.5	14.05	0.72138	0.00001	0.512109	0.000008	−10.32	0.15
790.5	14.65	0.72152	0.00001	0.512088	0.000008	−10.74	0.15
850.5	15.83	0.72144	0.00001	0.512077	0.000008	−10.94	0.15
901.0	17.09	0.72020	0.00001	0.512049	0.000007	−11.48	0.13
920.5	17.63	0.72213	0.00001	0.512088	0.000008	−10.73	0.16
991.0	19.46	0.72132	0.00001	0.512060	0.000007	−11.28	0.13
1000.5	19.68	0.72221	0.00001	0.512065	0.000008	−11.18	0.15
1060.5	21.36	0.72168	0.00001	0.512081	0.000008	−10.87	0.15
1100.5	22.52	0.72133	0.00001	0.512082	0.000008	−10.85	0.15
1150.5	23.96	0.72093	0.00001	0.512065	0.000008	−11.18	0.15
1201.0	25.42	0.72137	0.00001	0.512095	0.000008	−10.60	0.15
1261.0	26.93	0.72117	0.00001	0.512066	0.000011	−11.15	0.21
1300.5	27.67	0.72165	0.00001	0.512083	0.000008	−10.83	0.15
1340.5	28.43	0.72177	0.00001	0.512085	0.000008	−10.79	0.15
1370.5	28.99	0.72042	0.00001	0.512088	0.000008	−10.73	0.15
1411.0	29.75	0.72089	0.00001	0.512083	0.000008	−10.82	0.15
1460.5	30.68	0.72089	0.00001	0.512085	0.000008	−10.79	0.15

Clay mineralogical results for Core MD18-3569 are reported in a ternary diagram of (illite + chlorite)-kaolinite-smectite together with the mineralogical compositions of modern river sediments obtained using the same XRD analytical procedure (Liu et al., 2016) (Figure 7). The major proportions of illite (52%) and chlorite (32%) of Core MD18-3569 sediments are characteristic of assemblages related to illite and chlorite rich sediments from SW Taiwan rivers (56% illite and 36% chlorite) (Liu et al., 2016) (Figure 7). These results rule out the possibility that the Pearl River is the major source of clay to the studied site. First, the percentage of kaolinite is too low in the clay fraction of Core MD18-3569 (average 4%) to correspond to riverine sediment from South China (46%) and correspond instead to average kaolinite inputs from Taiwan rivers (4%) (Liu et al., 2016) (Figure 7). This could be the result of the Guangdong Coastal Current (GCC) and the westward circulation induced by the Kuroshio intrusion (Caruso et al., 2006) that transport sediments from the Pearl River southwards, along the Chinese continental shelf and/or the flocculation effect of kaolinite causing the mineral to sink and deposit on the continual shelf close to the mouth of the Pearl River (Xia et al., 2004). In addition, the illite crystallinity and illite chemistry index (0.158°Δ2θ and 0.324, respectively) obtained on the clay-size fraction of Core MD18-3569 is too low to be consistent with the high chemical weathering experienced by sediments in South China (0.198° Δ2θ and 0.466, respectively) (Liu et al., 2007) (Figure 8). Thus, SW Taiwan is the main source of illite and kaolinite for the studied site, while the input of sediments from the Pearl River can be considered negligible. Such results are

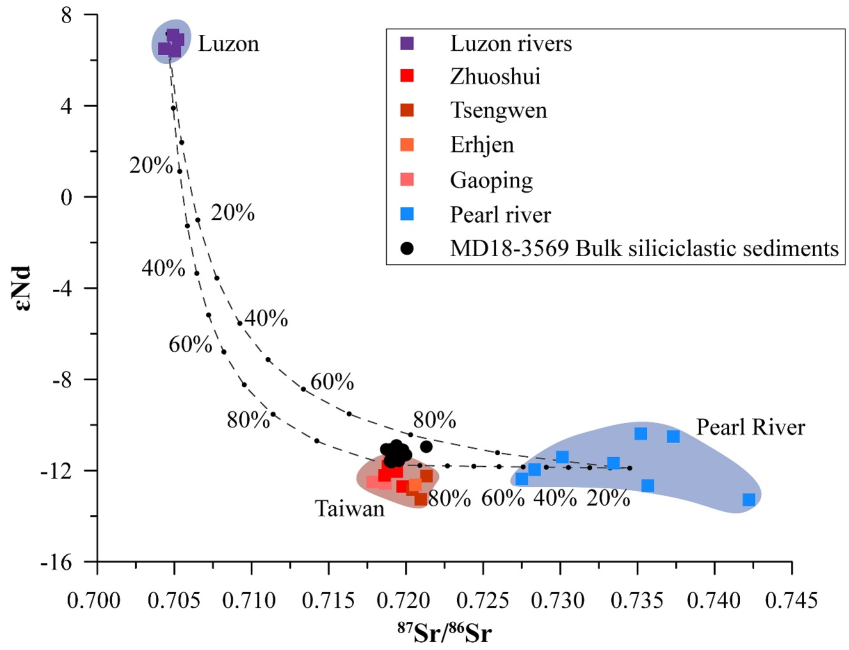

Figure 5. $^{87}Sr/^{86}Sr$ versus εNd diagram. $^{87}Sr/^{86}Sr$ ratios and εNd values obtained on the carbonate free-fractions of Core MD18-3569 (black dots, this study) are reported together with Sr and Nd isotopic compositions of Luzon rivers (purple squares) (Goldstein & Jacobsen, 1988; Liu et al., 2016), Pearl River (blue squares) (Liu et al., 2016), and SW Taiwan rivers (red squares) (Dou et al., 2016; Liu et al., 2016).

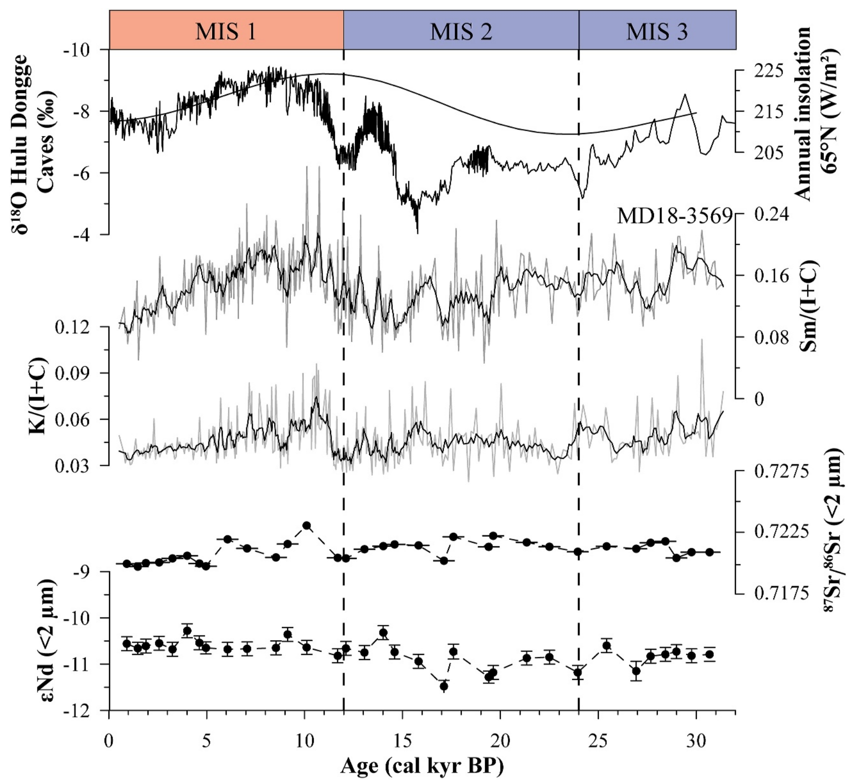

Figure 6. Temporal evolution of Sm/(I + C) and K/(I + C) mineralogical ratios and of $^{87}Sr/^{86}Sr$ ratio and εNd value obtained on the <2 µm siliciclastic fractions of Core MD18-3569. The insolation curve received by the earth at 65°N of latitude and the $\delta^{18}O$ record obtained on the Hulu and Dongge Cave speleothems (Dykoski et al., 2006; Wang et al., 2004) are reported for comparison.

10.1029/2023PA004745

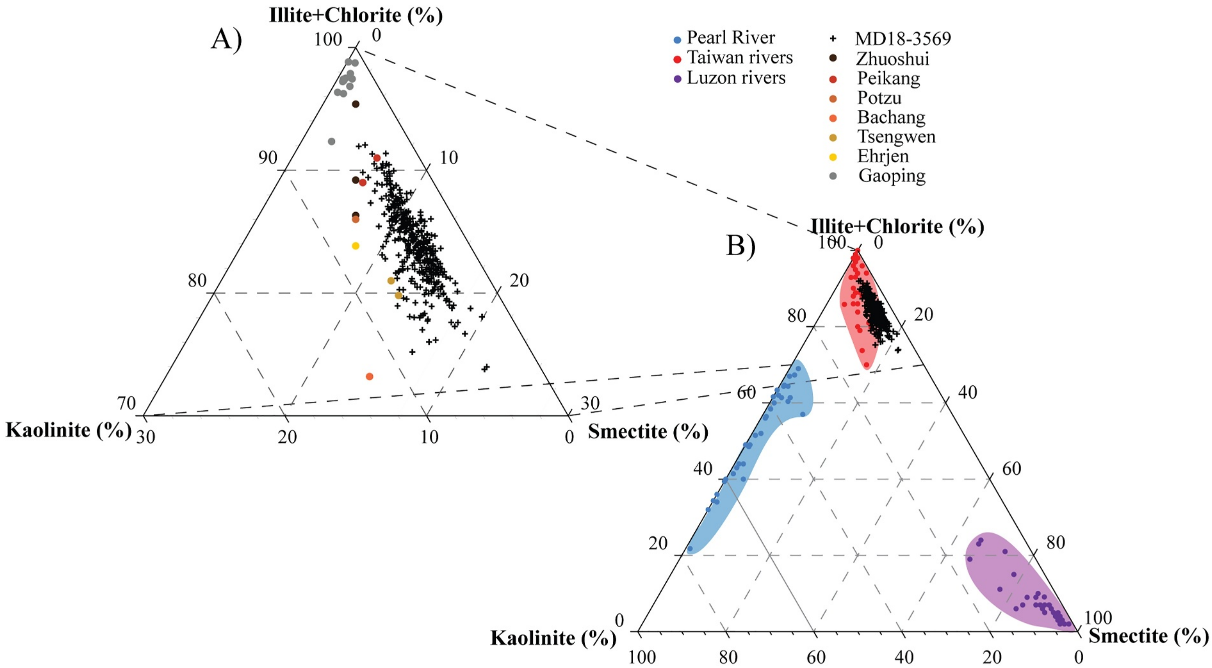

Figure 7. Ternary diagrams of major mineral groups of illite + chlorite, kaolinite, and smectite for Core MD18-3569 (a). Clay mineralogy compositions of surface sediments from Luzon rivers, Pearl River, and SW Taiwan rivers are included for comparison (Z. Liu et al., 2008, 2010, 2016). Zoomed plots for surface sediments of Taiwan rivers and Core MD18-3569 (b).

coherent with the Sr and Nd isotope results and the proximity of the study site to the southwestern coast of Taiwan and its river mouths.

However, the average smectite content (12%) of Core MD18-3569 is relatively high compared to the average of present-day inputs from SW Taiwan rivers to the SCS (4%) (Liu et al., 2016) (Figure 7). Such results are coherent with one previous study that also indicates that smectite proportions are higher in sediments of the Penghu

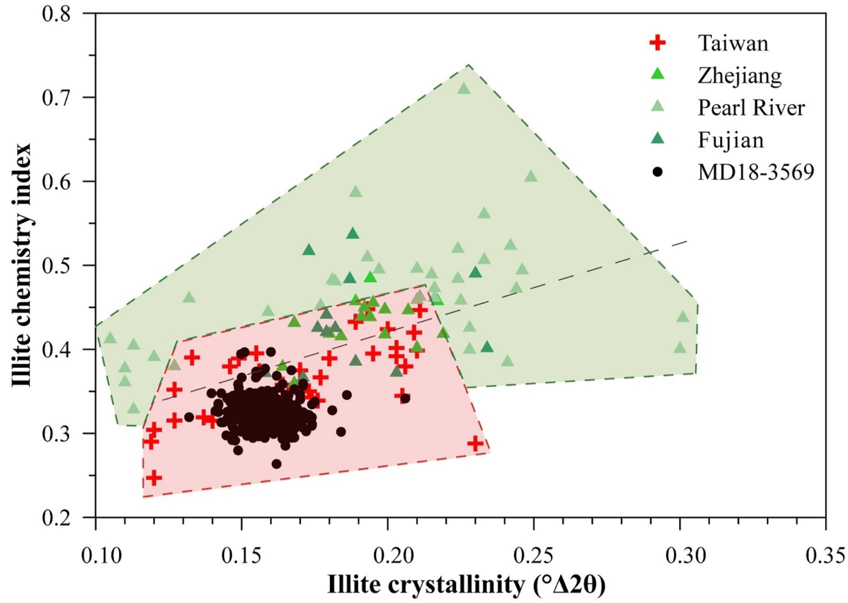

Figure 8. Illite crystallinity versus illite chemistry index of Core MD18-3569 (black dots) sediments compared to South China (green triangle) and Taiwan (red cross) river sediments (Liu et al., 2010, 2016).

Canyon system than those in the Gaoping Canyon, a fact that can be attributed to different land-sea configurations (Nayak et al., 2021). In fact, at present the Penghu Canyon is not directly connected to a river mouth but may have been connected, via the Penghu Channel, to the SW Taiwan rivers during low sea level intervals. This is in contrast with the Gaoping Canyon which has always been connected to the Gaoping River mouth, at least since the last glacial period (Yu et al., 2017). Taking this into account, we cannot fully exclude the possibility that a small portion of the smectite from Core MD18-3569 derives from a potential additional source. Another important source of smectite to the northeastern SCS is the basaltic province of Luzon and the volcanic formations of western Taiwan (Liu et al., 2009). However, higher proportions of smectite (or Sm/(I + C) ratio) are not systematically associated with more radiogenic εNd in the clay-size fraction. The $^{87}Sr/^{86}Sr$ ratios of the <2 μm fraction are even slightly higher during 10–6 cal kyr BP which contradicts the hypothesis of a greater volcanic contribution (Figure 6). Consequently, we can assume that the smectite does not derive from the weathering of volcanic formations but rather from crustal rocks on the island of Taiwan (Figure 6).

Several rivers located in western and southwestern Taiwan deliver moderate amounts of smectite to the SCS. These include Tsengwen (smectite content 15%) and Erhjen (smectite content 10%) rivers, which are close to the studied site, with sediment discharge of 9–16 Mt/yr and 21 Mt/yr, respectively, have some of the greatest sediment fluxes of all SW Taiwan rivers (Dadson et al., 2003). Figure 7 presents the clay mineral assemblages of the western and southwestern Taiwan rivers (Liu et al., 2010, 2016) in comparison to sediments from Core MD18-3569. It shows that most of the samples lie within the ranges of Tsengwen, Erhjen, and Bachang rivers, which are characterized by moderate smectite contents (8%–17%), suggesting that these rivers are potentially the main sources of fine sediments to Core MD18-3569. A minor portion of samples are distributed within the range of rivers with low to negligible smectite contents such as Potzu (smectite content 7%), Peikang (smectite content 6%), and Zhuoshui (smectite content 5%) rivers, which are located further north in western Taiwan. This suggests that a small number of fine sediments could also have derived from these western Taiwan rivers during the glacial low sea level stand when the strait was emerged (Figure 1). In such the low sea level condition, these rivers might have been directly connected to the Penghu Canyon system (Lambeck et al., 2014; Spratt & Lisiecki., 2016) (Figure 1). The sediments from core MD18-3569 are homogeneous and characterized by the absence of visible turbidites or erosion surfaces. This indicates that the sediments were mainly deposited by hemipelagic sedimentation and that the study site is not affected by the potential turbiditic activity of the Penghu Canyon in low and high sea-level period. Thus, the increase of sedimentation rate during the deglaciation and Holocene (Figure S1 in Supporting Information S1) is not associated with turbiditic activity but might be linked to terrigenous sediments supply and flux. The relatively stable εNd values and $^{87}Sr/^{86}Sr$ ratios of Core MD18-3569 sediments since 32 cal Kyr BP (Figure 5), suggest that the sediment provenance was not strongly affected by the sea-level rise and the land-sea reconfiguration during the deglaciation (Lambeck et al., 2014; Spratt & Lisiecki, 2016).

To sum up, clay mineral assemblages combined with the Nd and Sr isotopic compositions confirm that the SW Taiwan rivers (mainly Tsengwen and Erhjen rivers) have been the principal sources of sediments to Core MD18-3569 since the last glacial period. There is also a possible minor contribution of clay materials deriving from the rivers of western Taiwan (Zhuoshui, Bachang, Potzu, and Peikang rivers), which could have been transported to the SCS through the Taiwan Strait during the glacial low-sea level stand and derived to the study site.

5.2. Variations in Chemical Weathering and Physical Erosion of SW Taiwan

5.2.1. Deglaciation and Holocene Weathering Variations

Since SW Taiwan is the unique source of sediments to Core MD18-3569, the clay mineral assemblages and major element compositions of the core can be used to evaluate the state of chemical weathering of sediments transported to the study site (Clift et al., 2014; Hu et al., 2012; Huang et al., 2016; Liu et al., 2016; Wei et al., 2006). Major elements are reported in Al_2O_3–(CaO + Na_2O)–K_2O (A–CN–K) a ternary diagram to assess elemental leaching by chemical weathering (Figure 9). Sample distributions in the A–CN–K diagram indicate that sediments experienced moderate weathering in agreement with pronounced tectonic uplift of Taiwan which results in high rates of physical erosion. Such physical erosion conditions induce preferential leaching of Na and Ca and immobile Al and K, which is typical of Taiwan river sediments (Liu et al., 2016; Selvaraj & Chen, 2006). Thus, Na is compared to an immobile element, Al, through the Al_2O_3/Na_2O ratio. Hence a pronounced state of chemical weathering of sediments delivered to the study site from SW Taiwan will be associated with detrital material that

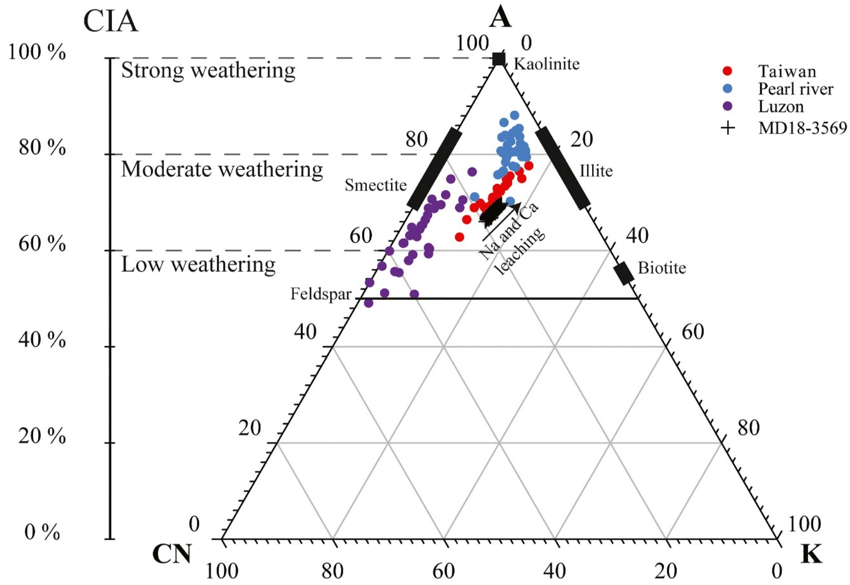

Figure 9. A–CN–K (Al_2O_3–($CaO + Na_2O$)–K_2O) ternary diagram plotting results obtained on Core MD18-3569 together with surface sediments from Luzon rivers (Liu et al., 2016), Pearl River (Liu et al., 2016), and SW Taiwan rivers (Liu et al., 2016) for comparison.

is relatively depleted in Na and enriched in Al leading to an increase in the Al_2O_3/Na_2O ratio (Selvaraj & Chen, 2006) (Figure 9).

Smectite/(illite + chlorite) (Sm/I + C), kaolinite/(illite + chlorite) (K/I + C), chemical index of alteration (CIA = molar ratio of $[Al_2O_3/(Al_2O_3 + Na_2O + K_2O + CaO^*) \times 100]$), Al_2O_3/SiO_2, and Al_2O_3/Na_2O are reported in Figure 10 as chemical weathering proxies. Smectite and, to a lesser extent, kaolinite contents display anti-covariations to illite and chlorite contents (Figure 3). As smectite and kaolinite are of the result of chemical weathering of primary minerals and illite and chlorite result from strong physical erosion, we can use Sm/(I + C) and K/(I + C) as proxies to establish past changes in the relative intensity of chemical weathering and physical erosion within the rivers basins of SW Taiwan. We can thus hypothesize that higher Sm/(I + C) and K/(I + C) ratios would suggest enhanced chemical weathering and/or a decrease in the physical erosion of the sedimentary sources.

The CIA can also be used to evaluate the state of chemical alteration of sediments (Clift et al., 2014; Colin et al., 2006; Hu et al., 2012; Liu et al., 2016). A CIA range of 80–100 indicates strong weathering, 80–60 indicates moderate weathering, 60–40 reflects low weathering, and values below 40 indicate no chemical weathering (Liu et al., 2016). CIA values for Core MD18-3569 range from 66 to 70 with an average value of 68 (Figure 10). This CIA values fall into the range of moderate chemical weathering values (80–60) and are in agreement with the A-CN-K ternary diagram (Figure 9). Finally, concentrations of Si in marine sediments are higher in the sand fraction (e.g., Quartz) than in the clay fraction, which is the product of grain-size sorting, where Al concentrations are high in the clay fraction, reflecting intense chemical weathering. Al_2O_3/SiO_2 variations can thus be attributed to changes in the relative proportion of clay and sand fractions and to siliciclastic discharge to the ocean linked to physical erosion versus chemical weathering on land (Clift et al., 2014). Clay minerals and bulk major elements were measured on different sediment fractions (<2 μm and bulk sediments). Clay minerals and the coarser minerals contained in bulk sediments respond differently to chemical weathering (e.g., quartz is considered to be more resistant to chemical weathering). Both proxies are resulting from slightly different chemical weathering degrees and processes and their variations can be slightly different.

The variations of CIA and Al_2O_3/Na_2O display slightly higher values during the MIS 3 than the Last Glacial Maximum (LGM) and an increasing trend from the LGM to the early Holocene. The minimum values of the CIA and Al_2O_3/Na_2O ratio occurred at 22 cal Kyr BP during the LGM and during the middle-late Holocene (Figure 10). Similar variations have been observed in the clay mineral assemblage with lower Sm/(I + C) and K/(I + C) ratios during the MIS2 compared to the MIS 3 and the early Holocene (between 11 and 5 cal Kyr BP).

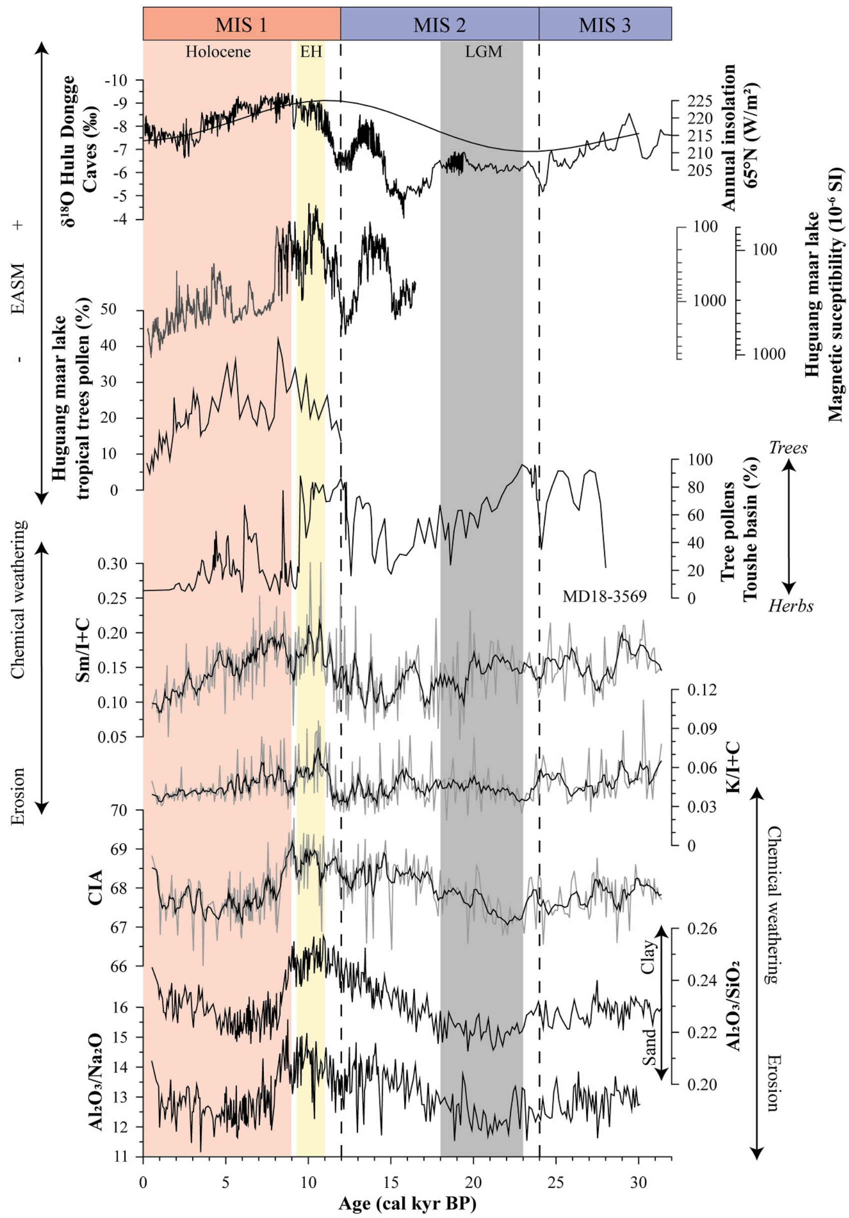

Figure 10. Temporal variations of erosional and weathering proxies of Core MD18-3569 for the past 32 Kyr: clay mineralogical Sm/(I + C) and K/(I + C), major elemental CIA, Al_2O_3/SiO_2, and Al_2O_3/Na_2O, in comparison to climatic $\delta^{18}O$ variations of Hulu and Dongge Cave speleothems (Dykoski et al., 2006; Wang et al., 2004), the insolation curve received by the earth at 65°N of latitude (Berger, 1978), magnetic susceptibility from Yanchi lake (Y. Li et al., 2017) and Huguang Maar lake (Yancheva et al., 2007), and pollen records from Toushe Basin (west Taiwan) (Sanchez Goñi et al., 2017) and Huguang Maar lake (South China) (Wang et al., 2007).

Such variations indicate that chemical weathering was relatively enhanced during the MIS3 compared to the LGM (and MIS2) when more clays were produced as indicated by the higher Al_2O_3/SiO_2 (Clift et al., 2014; Hu et al., 2012; Liu et al., 2016) (Figure 10). The LGM is thus characterized by a relatively weakened state of chemical weathering (lower Sm/(I + C) and K/(I + C), Si and Na-rich sediments with lower CIA) (Clift et al., 2014; Hu et al., 2012; Liu et al., 2016).

The continuous increase in proxies of weathering intensity (CIA, Al_2O_3/Na_2O, Sm/(I + C)) from the deglaciation to the beginning of the Holocene suggests a progressive enhancement of chemical weathering intensity during this period, with a maximum centered at 10 cal Kyr BP. The early-middle Holocene transition is characterized by a decreasing of proxies of weathering intensity from 9.2 to 8.7 cal Kyr BP; this trend is well marked in the CIA and the Al_2O_3/Na_2O ratio. The early to late Holocene is associated with a steady decrease of Sm/(I + C), K/(I + C), CIA, Al_2O_3/SiO_2, and Al_2O_3/Na_2O (Figure 10). This indicates a decrease in the state of chemical weathering of detrital material transported from the SW Taiwan basins to the northeastern SCS.

5.2.2. Role of the East Asian Monsoon and Typhoon Activity in Variations of Weathering in SW Taiwan

In Figure 10, chemical weathering proxy records of Core MD18-3569 are compared with $\delta^{18}O$ variations of Hulu and Dongge Cave speleothems (Dykoski et al., 2005; Wang et al., 2001), Huguang Maar lake (South China) magnetic susceptibility (Yancheva et al., 2007) and pollen record (Wang et al., 2007). These $\delta^{18}O$ stalagmites have been used to reconstruct past rainfall and winds in South China and the northeastern SCS region, 80% of which is generated by the EASM (Cheng et al., 2016; Dykoski et al., 2005; Liu et al., 2020; Wang et al., 2001). A negative shift of the $\delta^{18}O$ of the Hulu and Dongge Cave records corresponds to an increase in precipitation, while a period of more weakened EASM precipitation is characterized by a positive shift (Wang et al., 2001). However, $\delta^{18}O$ variations of speleothems significance has not reached consensus yet (Chen et al., 2022; Rao et al., 2016; Zhou et al., 2016). The chemical weathering record of Core MD18-3569 was also compared with speleothem independent proxies to ensure a relevant east Asian monsoon discussion. Climate has important control on vegetation, for example, tropical taxa are flourishing with warm and humid conditions. Wang et al. (2007) used tropical trees pollen proportions to reconstruct the moisture conditions in South China. Magnetic susceptibility of sediments from north and central China is commonly used as a proxy of the summer monsoon variation (e.g., An et al., 1991). In wet time intervals, the enhanced chemical weathering and pedogenesis of the loess, associated with the higher summer monsoon rainfall, favor the production of magnetic minerals (iron oxides) increasing the magnetic susceptibility values of sediments (An et al., 1991). During weak (strong) summer monsoon intervals, the stronger winter monsoon winds transport southward dusts from Chinese loess to South China (e.g., Huguang Maar lake). This results in an increase (decrease) of magnetic susceptibility values in South China sediments (Yancheva et al., 2007).

During the deglaciation and the early Holocene, clay mineralogical ratios (Sm/(I + C) and K/(I + C)) and elemental ratios (CIA, Al_2O_3/SiO_2, and Al_2O_3/Na_2O) increased, reaching a maximum at around 10 cal kyr BP. Thus, chemical weathering is increasing, and this can be correlated to a negative shift in the Hulu Dongge Cave $\delta^{18}O$, low values of magnetic susceptibility and high proportion of tropical trees pollen in South China resulting from intensified EASM rainfall (Figure 10). The deglaciation is characterized by a warming of east Asia, (e.g., Core MD18-3569 sea surface temperature warming (Chen et al., 2021) (Figure S1 in Supporting Information S1)). Studies suggest that the chemical weathering intensity increases with warmer temperature (Eppes et al., 2020). This could have also contributed to the deglaciation intensification of chemical weathering intensity in SW Taiwan.

The Holocene is characterized by a steady decrease of clay mineralogical ratios and leaching of mobile elements from 9 cal Kyr BP to its minimum at the present time. This interval of reduced chemical weathering agrees with the progressive decrease in the EASM precipitation observed in the $\delta^{18}O$ record of the Hulu Dongge cave, tropical trees pollen proportion and enhanced winter monsoon winds in South China (Figure 10) but not with the relatively stable SST recorded by Core MD18-3569 (Chen et al., 2021) (Figure S1 in Supporting Information S1). For Core MD18-3569, the state of chemical weathering of sediments recorded by Sm/(I + C) and K/(I + C) also displays a lower value interval, with minimum values occurring between 9.1 and 8.7 cal Kyr BP (Figure 10). This record is similar to the 9.2 Kyr EASM collapse described by W. Zhang et al. (2018) in a geochemical and pollen record from central China.

During the LGM, the clay mineral assemblage and major elements display less intensive chemical weathering than during the MIS3; this is in line with the shift to less negative $\delta^{18}O$ values resulting from weaker EASM precipitation. However, at a shorter time scale, rapid variations in the weathering proxies obtained on Core MD18-3569 (such as decreases of Sm/(I + C) centered at 17.5–16.8 cal Kyr BP, 15.5–14.5 cal Kyr BP, 13.5–13 cal Kyr BP, and 12.5–11.5 cal Kyr BP, Figure 10) are not associated with changes in monsoon rainfall as reconstructed from the Hulu Dongge cave $\delta^{18}O$, and Huguang Maar lake magnetic susceptibility records (Cheng et al., 2016; Dykoski et al., 2005; Wang et al., 2001; Yancheva et al., 2007). This suggests that the chemical weathering record is sensitive to the long term EASM trends but less sensitive to short time and millennial scale changes with the exception of the major monsoon collapse at 9.2 cal Kyr BP. Increased EASM precipitation slightly enhances the chemical weathering of sediments transferred from Taiwan to the northeastern SCS.

A pollen sequence from the Toushe Basin (west Taiwan) (Liew et al., 2006) is reported in Figure 10 and variations therein closely match those of the chemical weathering record obtained from Core MD18-3569 (Figure 10). Long term changes in tree pollen are coeval with the those of the Sm/(I + C) mineralogical ratio. The proportion of herb pollen versus tree pollen increases during the MIS2, between 24 and 15 cal Kyr BP, in agreement with colder and more arid conditions during this glacial time interval (Liew et al., 2006). Such variations in vegetation cover corroborate the LGM weakening of chemical weathering recorded by mineralogical (K/(I + C) and Sm/(I + C)) and geochemical (Al_2O_3/Na_2O, Al_2O_3/SiO_2, and CIA) ratios from Core MD18-3569 (Figure 10). Similarly, during the deglaciation (from 15 to 9.6 cal Kyr BP), contemporaneously with the increase of smectite and kaolinite production and leaching of Na and Ca (Figure 10), warmer and subtropical forests were becoming established in the Toushe Basin, reflected in an increase in the proportion of tree pollen present (Liew et al., 2006). This implies a warming up of climatic conditions and a strengthening of EASM rainfall (Cheng et al., 2016; Dykoski et al., 2005; Wang et al., 2001). Such climatic conditions and vegetation cover led to progressive pedogenesis and chemical weathering of soil (Arnaud et al., 2012; Bajard et al., 2016; Bajard, Poulenard, Sabatier, Develle, et al., 2017, Bajard, Poulenard, Sabatier, Etienne, et al., 2017; Sun & Colin, 2014). The short interval of weaker chemical weathering observed at about 9.2 cal Kyr BP is also associated in the pollen sequence with a drastic change in the vegetation cover, with relatively fewer trees and a higher proportion of herbs; this change has been attributed to the monsoon rainfall collapse event (Liew et al., 2006; W. Zhang et al., 2018). The time interval covering the middle and late Holocene is characterized by a decreasing trend in the proportion of trees pollen compared to herbs (Liew et al., 2006) indicating regressive pedogenesis (Arnaud et al., 2012; Bajard et al., 2016; Bajard, Poulenard, Sabatier, Develle, et al., 2017, Bajard, Poulenard, Sabatier, Etienne, et al., 2017; Sun & Colin, 2014) synchronous with the weakening of chemical weathering recorded by core MD18-3569 sediments (Figure 10). This interval is also marked by the weakening of the EASM (Cheng et al., 2016; Dykoski et al., 2005; Wang et al., 2001) which reduced chemical weathering. In addition, typhoons, which induce heavy precipitation events on the island of Taiwan, were shown to have been enhanced during the Holocene in the Pacific region (Chen et al., 2012; Moy et al., 2002; Wu, 1992; Zhou et al., 2019, 2021). Typhoon events induce intensive physical erosion of soils and rocks and rapid transport of sediment to the northeastern SCS through pronounced runoff (J. Liu et al., 2008; Wang et al., 2020; Xu et al., 2018). Recent studies have shown that typhoons and monsoon rainfall erosion affect chemical weathering intensity differently. The chemical weathering intensity associated with non-typhoon rainfall is coupled to the erosion intensity with a linear relationship (Lee et al., 2020). During typhoons, chemical weathering and erosion intensities do not follow a linear relationship, and chemical weathering intensity appears to be reduced with the increase of erosion compared to non-typhoon rainfall (Lee et al., 2020). However, typhoons frequency is considered to be associated with warm climate and intense summer monsoon and both induce rapid sediment transport, so clearly distinguishing typhoon and monsoon influence could be complicated (Clift, 2020). In present time, typhoons are triggering 70% of the turbidity currents on south Taiwan margin (Y. Zhang et al., 2018) and represent the majority of Taiwan sediments flux to the sea in recent times (~80%) (Lee et al., 2020). A turbidites record from Gaoping submarine canyon (south Taiwan) indicates turbidite frequency, and by extension typhoon events frequency, is increased after 7 ka and not associated with the monsoon weakening (Yu et al., 2017). Such typhoon events, coupled with the weakened EASM during the Holocene, are favorable to soil destabilization and regressive pedogenesis as has been observed in terrestrial palynological records (Liew et al., 2006). This gives rise to a shorter residence time of minerals in the soils of the SW Taiwan river basins and a progressive erosion of soils which, in turn, results in the delivery to the ocean of deeper horizons of less chemically altered soil material. In such conditions, detrital material transported to the SW Taiwan margin will have undergone less chemical weathering (lower CIA value and Al_2O_3/Na_2O ratio) than during the early Holocene time interval. Core MD18-3569 chemical weathering intensity (clay minerals and major elements) and Toushe Basin pollen records (Liew et al., 2006) show the important contribution of the temperature and east Asian monsoon rainfall variations to the chemical weathering intensity of SW Taiwan soils from the last glacial period to the early Holocene (Figure 10, Figure S1 in Supporting Information S1). Since the middle Holocene, the important typhoon activities appear to have a major impact on SW Taiwan sediments transport and weathering in comparison to monsoon or temperature. This is resulting in the increase of sediment discharge (high sedimentation rate (Figure S1 in Supporting Information S1)) and erosion enhancing the weakening of the chemical weathering associated with the EASM variations (Figure 10).

The chemical weathering record obtained from Core MD18-3569 indicates that the EASM has similar forcings on chemical weathering in SW Taiwan small rivers sediments with the large east Asian river basins (Chen et al., 2016; Sang et al., 2022) in opposition with what has been reported previously (Zhao et al., 2017). Taiwan chemical weathering degree of soils is strongly affected by the changes of regional East Asian and Pacific moisture transport.

6. Conclusions

Clay mineral assemblages, major elements, and Nd-Sr isotopes of detrital sediments from Core MD18-3569 on the eastern bank of the Penghu Canyon in the northeastern SCS have been investigated to identify sediment provenance and reconstruct changes in the degree of weathering of the sediments from the SW Taiwan and their potential links to climatic change since the last glacial period.

The clay mineral assemblage—consisting mainly of illite (average 52%) and chlorite (average 32%), with a moderate proportion of smectite (average 12%) and small quantities of kaolinite (average 4%) - combined with Nd and Sr isotopes (average −11.27 for εNd and average 0.719 for $^{87}Sr/^{86}Sr$) indicates that SW Taiwan is the sole source of sediment to Core MD18-3569.

Variations in clay mineral assemblage (Sm/(I + C), K/(I + C)) and major elements (CIA, Al_2O_3/Na_2O) allow us to evaluate the intensity of weathering in the SW Taiwan river basins in the past. The CIA (average 68) and A-CN-K diagram indicate that sediments have experienced moderate weathering which allows us to use the Al_2O_3/Na_2O ratio to track the weathering state of sediments. We have demonstrated that long term changes in the intensity of chemical weathering in the drainage basins of SW Taiwan is mainly driven by changes in EASM rainfall, temperature and environmental changes (pedogenesis) over the past 32 Kyr. The state of chemical weathering intensity of sediments transported to the SW Taiwan margin is modified by changes in vegetation cover. The time interval between 18 and 9 cal Kyr BP is characterized by a progressive increase in the intensity of chemical weathering, which reaches a maximum at the beginning of the Holocene (from 11 to 9 cal Kyr BP).

The state of chemical weathering of sediment transferred from SW Taiwan to the northeastern SCS decreases during the middle-late Holocene in agreement with a weakening of the EASM, a change in the vegetation cover (less tree pollen and a higher proportion of herbs) and an increase in typhoon activity. High typhoon activity and the changes in vegetation cover are favorable to soil destabilization, erosion, and regressive pedogenesis. In such conditions, detrital material transferred to the SW Taiwan margin will be less chemically weathered (lower CIA value and Al_2O_3/Na_2O ratio) due to minerals having a shorter residence time in the soils of SW Taiwan.

Data Availability Statement

Clay mineral and major element data involved in this study have been archived at the PANGAEA database (Bertaz et al., 2024a, 2024b).

Acknowledgments

We would like to thank the shipboard scientific party and the crew of R/V Marion Dufresne for their cooperation in collecting Core MD18-3569 during the HydroSed cruise (MD215) in 2018. We also thank Yuan Wang and Mingyang Yu from State Key Laboratory of Marine Geology (Tongji University) for laboratory assistance. We would specifically thank Editors Dr. Ursula Röhl and Dr. Yige Zhang and two anonymous reviewers for handling the manuscript and their thorough and insightful reviews. This work was supported by the National Natural Science Foundation of China (42188102, 42130407).

References

Adhikari, K., & Hartemink, A. E. (2016). Linking soils to ecosystem services—A global review. *Geoderma*, *262*, 101–111. https://doi.org/10.1016/j.geoderma.2015.08.009

An, Z., Kukla, G. J., Porter, S. C., & Xiao, J. (1991). Magnetic susceptibility evidence of monsoon variation on the Loess Plateau of central China during the last 130,000 years. *Quaternary Research*, *36*(1), 29–36. https://doi.org/10.1016/0033-5894(91)90015-W

An, Z., Wu, G., Li, J., Sun, Y., Liu, Y., Zhou, W., et al. (2015). Global monsoon dynamics and climate change. *Annual Review of Earth and Planetary Sciences*, *43*(1), 29–77. https://doi.org/10.1146/annurev-earth-060313-054623

Arnaud, F., Révillon, S., Debret, M., Revel, M., Chapron, E., Jacob, J., et al. (2012). Lake Bourget regional erosion patterns reconstruction reveals Holocene NW European Alps soil evolution and paleohydrology. *Quaternary Science Reviews*, *51*, 81–92. https://doi.org/10.1016/j.quascirev.2012.07.025

Bajard, M., Poulenard, J., Sabatier, P., Develle, A. L., Giguet-Covex, C., Jacob, J., et al. (2017). Progressive and regressive soil evolution phases in the Anthropocene. *Catena*, *150*, 39–52. https://doi.org/10.1016/j.catena.2016.11.001

Bajard, M., Poulenard, J., Sabatier, P., Etienne, D., Ficetola, F., Chen, W., et al. (2017). Long-term changes in alpine pedogenetic processes: Effect of millennial agro-pastoralism activities (French-Italian Alps). *Geoderma*, *306*, 217–236. https://doi.org/10.1016/j.geoderma.2017.07.005

Bajard, M., Sabatier, P., David, F., Develle, A. L., Reyss, J. L., Fanget, B., et al. (2016). Erosion record in Lake La Thuile sediments (Prealps, France): Evidence of montane landscape dynamics throughout the Holocene. *The Holocene*, *26*(3), 350–364. https://doi.org/10.1177/0959683615609750

Berger, A. (1978). Long-term variations of daily insolation and Quaternary climatic changes. *Journal of the Atmospheric Sciences*, *35*(12), 2362–2367. https://doi.org/10.1175/1520-0469(1978)035<2362:LTVODI>2.0.CO;2

Bertaz, J., Liu, Z., & Colin, C. (2024a). Clay minerals of sediment core MD18-3569 from the Penghu Canyon in the northeastern South China Sea. [Dataset]. *PANGAEA*. https://doi.org/10.1594/PANGAEA.964249

Bertaz, J., Liu, Z., & Colin, C. (2024b). Major elements of sediment core MD18-3569 from the Penghu Canyon in the northeastern South China Sea. [Dataset]. *PANGAEA*. https://doi.org/10.1594/PANGAEA.964251

Bi, L., Yang, S., Li, C., Guo, Y., Wang, Q., Liu, J.-T., & Yin, P. (2015). Geochemistry of river-borne clays entering the East China Sea indicates two contrasting types of weathering and sediment transport processes. Geochem. *Geochemistry, Geophysics, Geosystems*, *16*(9), 3034–3052. https://doi.org/10.1002/2015GC005867

Boulay, S., Colin, C., Trentesaux, A., Clain, S., Liu, Z., & Lauer-Leredde, C. (2007). Sedimentary responses to the Pleistocene climatic variations recorded in the South China Sea. *Quaternary Research*, *68*(1), 162–172. https://doi.org/10.1016/j.yqres.2007.03.00

Boulay, S., Colin, C., Trentesaux, A., Frank, N., & Liu, Z. (2005). Sediment sources and East Asian monsoon intensity over the last 450 ky. Mineralogical and geochemical investigations on South China Sea sediments. *Palaeogeography, Palaeoclimatology, Palaeoecology*, *228*(3–4), 260–277. https://doi.org/10.1016/j.palaeo.2005.06.005

Braconnot, P., Marzin, C., Grégoire, L., Mosquet, E., & Marti, O. (2008). Monsoon response to changes in Earth's orbital parameters: Comparisons between simulations of the Eemian and of the Holocene. *Climate of the Past*, *4*(4), 281–294. https://doi.org/10.5194/cp-4-281-2008

Brantley, S. L., Goldhaber, M. B., & Ragnarsdottir, K. V. (2007). Crossing disciplines and scales to understand the critical zone. *Elements*, *3*(5), 307–314. https://doi.org/10.2113/gselements.3.5.307

Brantley, S. L., McDowell, W. H., Dietrich, W. E., White, T. S., Kumar, P., Anderson, S. P., et al. (2017). Designing a network of critical zone observatories to explore the living skin of the terrestrial Earth. *Earth Surface Dynamics*, *5*(4), 841–860. https://doi.org/10.5194/esurf-5-841-2017

Bull, W. B. (1990). Stream-terrace genesis: Implications for soil development. *Geomorphology*, *3*(3–4), 351–367. https://doi.org/10.1016/0169-555X(90)90011-E

Caruso, M. J., Gawarkiewicz, G. G., & Beardsley, R. C. (2006). Interannual variability of the Kuroshio intrusion in the South China Sea. *Journal of Oceanography*, *62*(4), 559–575. https://doi.org/10.1007/s10872-006-0076-0

Chen, H. F., Wen, S. Y., Song, S. R., Yang, T. N., Lee, T. Q., Lin, S. F., et al. (2012). Strengthening of paleo-typhoon and autumn rainfall in Taiwan corresponding to the Southern Oscillation at late Holocene. *Journal of Quaternary Science*, *27*(9), 964–972. https://doi.org/10.1002/jqs.2590

Chen, Q., Cheng, X., Cai, Y., Luo, Q., Zhang, J., Tang, L., et al. (2022). Asian summer monsoon changes inferred from a stalagmite δ18O record in Central China during the Last Glacial Period. *Frontiers in Earth Science*, *10*. https://doi.org/10.3389/feart.2022.863829

Chen, Y., Wang, Y., Dang, H., & Jian, Z. (2021). Hydroclimatic changes in the northeastern South China Sea since the Last Glacial Maximum. *Quaternary Sciences*, *41*(4), 1031–1043. https://doi.org/10.11928/j.issn.1001-7410.2021.04.13

Chen, Z., Ding, Z., Yang, S., Zhang, C., & Wang, X. (2016). Increased precipitation and weathering across the Paleocene-eocene thermal maximum in central China. *Geochemistry, Geophysics, Geosystems*, *17*(6), 2286–2297. https://doi.org/10.1002/2016GC006333

Cheng, H., Edwards, R. L., Sinha, A., Spötl, C., Yi, L., Chen, S., et al. (2016). The Asian monsoon over the past 640,000 years and ice age terminations. *Nature*, *534*(7609), 640–646. https://doi.org/10.1038/nature18591

Ching, K. E., Hsieh, M. L., Johnson, K. M., Chen, K. H., Rau, R. J., & Yang, M. (2011). Modern vertical deformation rates and mountain building in Taiwan from precise leveling and continuous GPS observations, 2000-2008. *Journal of Geophysical Research*, *116*(B8), B08406. https://doi.org/10.1029/2011JB008242

Clift, P. D. (2020). Asian monsoon dynamics and sediment transport in SE Asia. *Journal of Asian Earth Sciences*, *195*, 104352. https://doi.org/10.1016/j.jseaes.2020.104352

Clift, P. D., & Sun, Z. (2006). The sedimentary and tectonic evolution of the Yinggehai–Song Hong basin and the southern Hainan margin, South China Sea: Implications for Tibetan uplift and monsoon intensification. *Journal of Geophysical Research*, *111*(B6). https://doi.org/10.1029/2005JB004048

Clift, P. D., Wan, S., & Blusztajn, J. (2014). Reconstructing chemical weathering, physical erosion and monsoon intensity since 25 Ma in the northern South China Sea: A review of competing proxies. *Earth-Science Reviews*, *130*, 86–102. https://doi.org/10.1016/j.earscirev.2014.01.002

Colin, C., Siani, G., Sicre, M. A., & Liu, Z. (2010). Impact of the East Asian monsoon rainfall changes on the erosion of the Mekong River basin over the past 25,000 yr. *Marine Geology*, *271*(1–2), 84–92. https://doi.org/10.1016/j.margeo.2010.01.013

Colin, C., Turpin, L., Bertaux, J., Desprairies, A., & Kissel, C. (1999). Erosional history of the Himalayan and Burman ranges during the last two glacial–interglacial cycles. *Earth and Planetary Science Letters*, *171*(4), 647–660. https://doi.org/10.1016/S0012-821X(99)00184-3

Colin, C., Turpin, L., Blamart, D., Frank, N., Kissel, C., & Duchamp, S. (2006). Evolution of weathering patterns in the Indo-Burman Ranges over the last 280 kyr: Effects of sediment provenance on 87Sr/86Sr ratios tracer. *Geochemistry, Geophysics, Geosystems*, *7*(3). https://doi.org/10.1029/2005GC000962

Copard, K., Colin, C., Douville, E., Freiwald, A., Gudmundsson, G., De Mol, B., & Frank, N. (2010). Nd isotopes in deep-sea corals in the North-eastern Atlantic. *Quaternary Science Reviews*, *29*(19–20), 2499–2508. https://doi.org/10.1016/j.quascirev.2010.05.025

Dadson, S. J., Hovius, N., Chen, H., Dade, W. B., Hsieh, M. L., Willett, S. D., et al. (2003). Links between erosion, runoff variability and seismicity in the Taiwan orogen. *Nature*, *426*(6967), 648–651. https://doi.org/10.1038/nature02150

Ding, X., Zheng, L., Li, D., Yang, T. N., Lee, T. Q., & Kao, S. J. (2016). Lacustrine record of centennial-and millennial-scale rainfall variability of the East Asian summer monsoon during the last deglaciation: Multi-proxy evidence from Taiwan. *Palaeogeography, Palaeoclimatology, Palaeoecology*, *450*, 38–49. https://doi.org/10.1016/j.palaeo.2016.02.048

Dosseto, A., Hesse, P. P., Maher, K., Fryirs, K., & Turner, S. (2010). Climatic and vegetation control on sediment dynamics during the last glacial cycle. *Geology*, *38*(5), 395–398. https://doi.org/10.1130/G30708.1

Dou, Y., Yang, S., Shi, X., Clift, P. D., Liu, S., Liu, J., et al. (2016). Provenance weathering and erosion records in southern Okinawa Trough sediments since 28 ka: Geochemical and Sr–Nd–Pb isotopic evidences. *Chemical Geology*, *425*, 93–109. https://doi.org/10.1016/j.chemgeo.2016.01.029

Dykoski, C. A., Edwards, R. L., Cheng, H., Yuan, D., Cai, Y., Zhang, M., et al. (2005). A high-resolution, absolute-dated Holocene and deglacial Asian monsoon record from Dongge Cave, China. *Earth and Planetary Science Letters*, *233*(1–2), 71–86. https://doi.org/10.1016/j.epsl.2005.01.036

Dykoski, C. A., Edwards, R. L., Cheng, H., Yuan, D., Cai, Y., Zhang, M., et al. (2006). Dongge cave stalagmite Holocene and deglacial oxygen isotope data. [Dataset]. *IGBP PAGES/World Data Center for Paleoclimatology Data Contribution Series # 2006-099*. https://doi.org/10.25921/fptc-th03

Eppes, M. C., Magi, B., Scheff, J., Warren, K., Ching, S., & Feng, T. (2020). Warmer, wetter climates accelerate mechanical weathering in field data, independent of stress loading. *Geophysical Research Letters*, *47*(24), GL089062. https://doi.org/10.1029/2020GL089062

Fang, G., Fang, W., Fang, Y., & Wang, K. (1998). A survey of studies on the South China Sea upper ocean circulation. *Acta Oceanographica Taiwanica*, *37*, 1–16.

Gaillardet, J., Braud, I., Hankard, F., Anquetin, S., Bour, O., Dorfliger, N., et al. (2018). OZCAR: The French network of critical zone observatories. *Vadose Zone Journal*, *17*(1), 1–24. https://doi.org/10.2136/vzj2018.04.0067

Gan, J., Liu, Z., & Hui, C. R. (2016). A three-layer alternating spinning circulation in the South China Sea. *Journal of Physical Oceanography*, *46*(8), 2309–2315. https://doi.org/10.1175/JPO-D-16-0044.1

Gebregiorgis, D., Hathorne, E. C., Sijinkumar, A. V., Nath, B. N., Nürnberg, D., & Frank, M. (2016). South Asian summer monsoon variability during the last~ 54 kyrs inferred from surface water salinity and river runoff proxies. *Quaternary Science Reviews*, *138*, 6–15. https://doi.org/10.1016/j.quascirev.2016.02.012

Goldstein, S. J., & Jacobsen, S. B. (1988). Nd and Sr isotopic systematics of river water suspended material: Implications for crustal evolution. *Earth and Planetary Science Letters*, *87*(3), 249–265. https://doi.org/10.1016/0012-821X(88)90013-1

Hsieh, M. L., & Knuepfer, P. L. (2001). Middle–late Holocene river terraces in the Erhjen river basin, southwestern Taiwan—Implications of river response to climate change and active tectonic uplift. *Geomorphology*, *38*(3–4), 337–372. https://doi.org/10.1016/S0169-555X(00)00105-7

Hsieh, M. L., & Knuepfer, P. L. (2002). Synchroneity and morphology of Holocene river terraces in the southern western Foothills, Taiwan: A guide to interpreting and correlating erosional river terraces across growing anticlines. *Geological Society of America Special Paper*, *358*, 55–74. https://doi.org/10.1130/0-8137-2358-2.55

Hu, B., Li, J., Cui, R., Wei, H., Zhao, J., Li, G., et al. (2014). Clay mineralogy of the riverine sediments of Hainan Island, South China Sea: Implications for weathering and provenance. *Journal of Asian Earth Sciences*, *96*, 84–92. https://doi.org/10.1016/j.jseaes.2014.08.03

Hu, D., Böning, P., Köhler, C. M., Hillier, S., Pressling, N., Wan, S., et al. (2012). Deep sea records of the continental weathering and erosion response to East Asian monsoon intensification since 14 ka in the South China Sea. *Chemical Geology*, *326*, 1–18. https://doi.org/10.1016/j.chemgeo.2012.07.024

Hu, J., Kawamura, H., Hong, H., & Qi, Y. (2000). A review on the currents in the South China Sea: Seasonal circulation, South China sea warm current and Kuroshio intrusion. *Journal of Oceanography*, *56*(6), 607–624. https://doi.org/10.1023/A:1011117531252

Hu, S., Zeng, Z., Fang, X., Yin, X., Chen, Z., Li, X., et al. (2020). Increasing terrigenous sediment supply from Taiwan to the southern Okinawa Trough over the last 3000 years evidenced by SrNd isotopes and geochemistry. *Sedimentary Geology*, *406*, 105725. https://doi.org/10.1016/j.sedgeo.2020.105725

Huang, C. Y., Wu, W. Y., Chang, C. P., Tsao, S., Yuan, P.-B., Lin, C. W., & Xia, K. Y. (1997). Tectonic evolution of accretionary prism in the arc-continent collision terrane of Taiwan. *Tectonophysics*, *281*(1–2), 31–51. https://doi.org/10.1016/S0040-1951(97)00157-1

Huang, J., Wan, S., Xiong, Z., Zhao, D., Liu, X., Li, A., & Li, T. (2016). Geochemical records of Taiwan-sourced sediments in the South China Sea linked to Holocene climate changes. *Palaeogeography, Palaeoclimatology, Palaeoecology*, *441*, 871–881. https://doi.org/10.1016/j.palaeo.2015.10.036

Innocent, C., Fagel, N., & Hillaire-Marcel, C. (2000). Sm–Nd isotope systematics in deep-sea sediments: Clay-size versus coarser fractions. *Marine Geology*, *168*(1–4), 79–87. https://doi.org/10.1016/S0025-3227(00)00052-9

Jacobsen, S. B., & Wasserburg, G. J. (1980). Sm-Nd isotopic evolution of chondrites. *Earth and Planetary Science Letters*, *50*(1), 139–155. https://doi.org/10.1016/0012-821X(80)90125-9

Jiwarungrueangkul, T., Liu, Z., Stattegger, K., & Sang, P. N. (2019). Reconstructing chemical weathering intensity in the Mekong river basin since the last Glacial Maximum. *Palaeogeography, and Palaeoclimatology.*, *34*(11), 1710–1725. https://doi.org/10.1029/2019PA003608

Lambeck, K., Rouby, H., Purcell, A., Sun, Y., & Sambridge, M. (2014). Sea level and global ice volumes from the Last Glacial Maximum to the Holocene. *Proceedings of the National Academy of Sciences of the United States of America*, *111*(43), 15296–15303. https://doi.org/10.1073/pnas.1411762111

Latour, B. (2014). Some advantages of the notion of "Critical Zone" for geopolitics. *Procedia Earth and Planetary Science*, *10*, 3–6. https://doi.org/10.1016/j.proeps.2014.08.002

Lee, Y. J., Chen, P. H., Lee, T. Y., Shih, Y. T., & Huang, J. C. (2020). Temporal variation of chemical weathering rate, source shifting and relationship with physical erosion in small mountainous rivers, Taiwan. *Catena*, *190*, 104516. https://doi.org/10.1016/j.catena.2020.104516

Lei, C., Ren, J., Sternai, P., Fox, M., Willett, S., Xie, X., et al. (2015). Structure and sediment budget of Yinggehai–Song Hong basin, South China Sea: Implications for Cenozoic tectonics and river basin reorganization in Southeast Asia. *Tectonophysics*, *655*, 177–190. https://doi.org/10.1016/j.tecto.2015.05.024

Li, L., & Qu, T. (2006). Thermohaline circulation in the deep South China Sea basin inferred from oxygen distributions. *Journal of Geophysical Research*, *111*(C5). https://doi.org/10.1029/2005JC003164

Li, Y., Wang, N., Li, Z., Zhou, X., & Zhang, C. (2017). NOAA/WDS paleoclimatology - Yanchi Lake, northwest China 16,000 year geochemical data [Dataset]. *NOAA National Centers for Environmental Information*. https://doi.org/10.25921/rsdz-5b03

Liew, P.-M., Huang, S.-Y., & Kuo, C.-M. (2006). Pollen stratigraphy, vegetation and environment of the last glacial and Holocene—A record from Toushe Basin, central Taiwan. *Quaternary International*, *147*(1), 16–33. https://doi.org/10.1016/j.quaint.2005.09.003

Liu, J. P., Liu, C. S., Xu, K. H., Milliman, J. D., Chiu, J. K., Kao, S. J., & Lin, S. W. (2008). Flux and fate of small mountainous rivers derived sediments into the Taiwan Strait. *Marine Geology*, *256*(1–4), 65–76. https://doi.org/10.1016/j.margeo.2008.09.007

Liu, X., Liu, J., Chen, S., Chen, J., Zhang, X., Yan, J., & Chen, F. (2020). New insights on Chinese cave $\delta^{18}O$ records and their paleoclimatic significance. *Earth-Science Reviews*, *207*, 103216. https://doi.org/10.1016/j.earscirev.2020.103216

Liu, Z., Colin, C., Huang, W., Chen, Z., Trentesaux, A., & Chen, J. (2007). Clay minerals in surface sediments of the Pearl River drainage basin and their contribution to the South China Sea. *Chinese Science Bulletin*, *52*(8), 1101–1111. https://doi.org/10.1007/s11434-007-0161-9

Liu, Z., Colin, C., Li, X., Zhao, Y., Tuo, S., Chen, Z., et al. (2010). Clay mineral distribution in surface sediments of the northeastern South China Sea and surrounding fluvial drainage basins: Source and transport. *Marine Geology*, *277*(1–4), 48–60. https://doi.org/10.1016/j.margeo.2010.08.010

Liu, Z., Colin, C., Trentesaux, A., Blamart, D., Bassinot, F., Siani, G., & Sicre, M. A. (2004). Erosional history of the eastern Tibetan Plateau since 190 kyr ago: Clay mineralogical and geochemical investigations from the southwestern South China Sea. *Marine Geology*, *209*(1–4), 1–18. https://doi.org/10.1016/j.margeo.2004.06.004

Liu, Z., Colin, C., Trentesaux, A., Siani, G., Frank, N., Blamart, D., & Farid, S. (2005). Late Quaternary climatic control on erosion and weathering in the eastern Tibetan Plateau and the Mekong Basin. *Quaternary Research*, *63*(3), 316–328. https://doi.org/10.1016/j.yqres.2005.02.005

Liu, Z., Tuo, S., Colin, C., Liu, J.-T., Huang, C.-Y., Selvaraj, K., et al. (2008). Detrital fine-grained sediment contribution from Taiwan to the northern South China Sea and its relation to regional ocean circulation. *Marine Geology*, *255*(3–4), 149–155. https://doi.org/10.1016/j.margeo.2008.08.003

Liu, Z., Zhao, Y., Colin, C., Siringan, F. P., & Wu, Q. (2009). Chemical weathering in Luzon, Philippines from clay mineralogy and major-element geochemistry of river sediments. *Applied Geochemistry*, *24*(11), 2195–2205. https://doi.org/10.1016/j.apgeochem.2009.09.025

Liu, Z., Zhao, Y., Colin, C., Stattegger, K., Wiesner, M.-G., Huh, C.-A., et al. (2016). Source-to-sink transport processes of fluvial sediments in the South China Sea. *Earth-Science Reviews*, *153*, 238–273. https://doi.org/10.1016/j.earscirev.2015.08.005

Lugmair, G. W., Shimamura, T., Lewis, R. S., & Anders, E. (1983). Samarium-146 in the early solar system: Evidence from neodymium in the Allende meteorite. *Science*, *222*(4627), 1015–1018. https://doi.org/10.1126/science.222.4627.1015

Meyer, I., Davies, G. R., & Stuut, J. B. W. (2011). Grain size control on Sr-Nd isotope provenance studies and impact on paleoclimate reconstructions: An example from deep-sea sediments offshore NW Africa. *Geochemistry, Geophysics, Geosystems*, *12*(3). https://doi.org/10.1029/2010GC003355

Milliman, J. D., & Farnsworth, K. L. (2011). *River discharge to the coastal ocean: A global synthesis*. Cambridge University Press.

Milliman, J. D., & Syvitski, J. P. (1992). Geomorphic/tectonic control of sediment discharge to the ocean: The importance of small mountainous rivers. *The Journal of Geology*, *100*(5), 525–544. https://doi.org/10.1086/629606

Miriyala, P., Sukumaran, N. P., Nath, B. N., Ramamurty, P. B., Sijinkumar, A. V., Vijayagopal, B., et al. (2017). Increased chemical weathering during the deglacial to mid-Holocene summer monsoon intensification. *Scientific Reports*, *7*(1), 1–11. https://doi.org/10.1038/srep44310

Molnar, P. (2001). Climate change, flooding in arid environments, and erosion rates. *Geology*, *29*(12), 1071–1074. https://doi.org/10.1130/0091-7613(2001)029<1071:CCFIAE>2.0.CO;2

Moy, C. M., Seltzer, G. O., Rodbell, D. T., & Anderson, D. M. (2002). Variability of El Niño/Southern Oscillation activity at millennial timescales during the Holocene epoch. *Nature*, *420*(6912), 162–165. https://doi.org/10.1038/nature01194

Nayak, K., Lin, A. T. S., Huang, K. F., Liu, Z., Babonneau, N., Ratzov, G., et al. (2021). Clay-mineral distribution in recent deep-sea sediments around Taiwan: Implications for sediment dispersal processes. *Tectonophysics*, *814*, 228974. https://doi.org/10.1016/j.tecto.2021.228974

Qu, T., Girton, J. B., & Whitehead, J. A. (2006). Deepwater overflow through Luzon strait. *Journal of Geophysical Research*, *111*(C1). https://doi.org/10.1029/2005JC003139

Rao, Z., Li, Y., Zhang, J., Jia, G., & Chen, F. (2016). Investigating the long-term palaeoclimatic controls on the δD and δ18O of precipitation during the Holocene in the Indian and East Asian monsoonal regions. *Earth-Science Reviews*, *159*, 292–305. https://doi.org/10.1016/j.earscirev.2016.06.007

Rasmusson, E. M., & Carpenter, T. H. (1982). Variations in tropical sea surface temperature and surface wind fields associated with the Southern Oscillation/El Niño. *Monthly Weather Review*, *110*(5), 354–384. https://doi.org/10.1175/1520-0493(1982)110<0354:VITSST>2.0.CO;2

Riebe, C. S., Kirchner, J. W., Granger, D. E., & Finkel, R. C. (2001). Strong tectonic and weak climatic control of long-term chemical weathering rates. *Geology*, *29*(6), 511–514. https://doi.org/10.1130/0091-7613(2001)029<0511:STAWCC>2.0.CO;2

Ruddiman, W. (2001). *Earth's climate: Past and Future*. W. H. Freeman and Company. https://doi.org/10.1016/S0921-8181(01)00108-4

Sabatier, P., Poulenard, J., Fanget, B., Reyss, J. L., Develle, A. L., Wilhelm, B., et al. (2014). Long-term relationships among pesticide applications, mobility, and soil erosion in a vineyard watershed. *Proceedings of the National Academy of Sciences of the United States of America*, *111*(44), 15647–15652. https://doi.org/10.1073/pnas.1411512111

Sanchez Goñi, M. F., Desprat, S., Daniau, A. A. L., Liew, P. M., Huang, S. Y., & Kuo, C. M. (2017). CLAM age model and pollen profile of sediment core Toushe_Basin. [Dataset]. *PANGAEA*. https://doi.org/10.1594/PANGAEA.872916

Sang, P. N., Liu, Z., & Colin, C. (2022). Chemical weathering of the Mekong river basin with implication for East Asian monsoon evolution during the late quaternary: Marine sediment records in the southern South China Sea. *Frontiers in Earth Science*, *10*, 1027. https://doi.org/10.3389/feart.2022.885547

Sang, P. N., Liu, Z., Zhao, Y., Zhao, X., Pha, P. D., & Van Long, H. (2018). Chemical weathering in central Vietnam from clay mineralogy and major-element geochemistry of sedimentary rocks and river sediments. *Heliyon*, *4*(7), e00710. https://doi.org/10.1016/j.heliyon.2018.e00710

Selvaraj, K., & Chen, C. T. A. (2006). Moderate chemical weathering of subtropical Taiwan: Constraints from solid-phase geochemistry of sediments and sedimentary rocks. *The Journal of Geology*, *114*(1), 101–116. https://doi.org/10.1086/498102

Selvaraj, K., Chen, C. T. A., & Lou, J. Y. (2007). Holocene East Asian monsoon variability: Links to solar and tropical Pacific forcing. *Geophysical Research Letters*, *34*(1). https://doi.org/10.1029/2006GL028155

Singh, M., Sharma, M., & Tobschall, H. J. (2005). Weathering of the Ganga alluvial plain, northern India: Implications from fluvial geochemistry of the Gomati river. *Applied Geochemistry*, *20*(1), 1–21. https://doi.org/10.1016/j.apgeochem.2004.07.005

Spratt, R. M., & Lisiecki, L. E. (2016). A Late Pleistocene sea level stack. *Climate of the Past*, *12*(4), 1079–1092. https://doi.org/10.5194/cp-12-1079-2016

Sun, Q., & Colin, C. (2014). Paleoclimate and Paleoenvironment of Gonghe basin, Qinghai-Tibet Plateau, during the Lastdeglacial: Weathering, erosion and vegetation cover affect clay mineral formation. *Acta Geologica Sinica*, *88*(2), 647–660. https://doi.org/10.1111/1755-6724.12220

Tanaka, T., Togashi, S., Kamioka, H., Amakawa, H., Kagami, H., Hamamoto, T., et al. (2000). JNdi-1: A neodymium isotopic reference in consistency with LaJolla neodymium. *Chemical Geology*, *168*(3–4), 279–281. https://doi.org/10.1016/S0009-2541(00)00198-4

Tian, J., Yang, Q., Liang, X., Xie, L., Hu, D., Wang, F., & Qu, T. (2006). Observation of Luzon strait transport. *Geophysical Research Letters*, *33*(19). https://doi.org/10.1029/2006GL026272

Wang, G., Xie, S.-P., Qu, T., & Huang, R. X. (2011). Deep South China Sea circulation. *Geophysical Research Letters*, *38*(5). https://doi.org/10.1029/2010GL046626

Wang, L. C., Behling, H., Kao, S. J., Li, H. C., Selvaraj, K., Hsieh, M. L., & Chang, Y. P. (2015). Late Holocene environment of subalpine northeastern Taiwan from pollen and diatom analysis of lake sediments. *Journal of Asian Earth Sciences*, *114*, 447–456. https://doi.org/10.1016/j.jseaes.2015.03.037

Wang, M., Shao, Y., Jiang, Q. O., Xiao, L., Yan, H., Gao, X., et al. (2020). Impacts of climate change and human activity on the runoff changes in the Guishui River Basin. *Land*, *9*(9), 291. https://doi.org/10.3390/land9090291

Wang, P., Jian, Z., Zhao, Q., Li, Q., Wang, R., Liu, Z., et al. (2003). Evolution of the South China Sea and monsoon history revealed in deep-sea records. *Chinese Science Bulletin*, *48*(23), 2549–2561. https://doi.org/10.1360/03wd0156

Wang, P., Wang, B., Cheng, H., Fasullo, J., Guo, Z., Kiefer, T., & Liu, Z. (2017). The global monsoon across time scales: Mechanisms and outstanding issues. *Earth-Science Reviews*, *174*, 84–121. https://doi.org/10.1016/j.earscirev.2017.07.006

Wang, S., Lü, H., Liu, J., & Negendank, J. F. W. (2007). The early Holocene optimum inferred from a high-resolution pollen record of Huguangyan Maar Lake in southern China. *Chinese Science Bulletin*, *52*(20), 2829–2836. https://doi.org/10.1007/s11434-007-0419-2

Wang, Y. J., Cheng, H., Edwards, R. L., An, Z. S., Wu, J. Y., Shen, C. C., & Dorale, J. A. (2001). A high-resolution absolute-dated late Pleistocene monsoon record from Hulu Cave, China. *Science*, *294*(5550), 2345–2348. https://doi.org/10.1126/science.1064618

Wang, Y. J., Cheng, H., Edwards, R. L., An, Z. S., Wu, J. Y., Shen, C. C., & Dorale, J. A. (2004). Hulu cave stalagmite oxygen isotope data. [Dataset]. *IGBP PAGES/World Data Center for Paleoclimatology Data Contribution Series #2004-023*. https://doi.org/10.25921/h9ed-1h93

Webster, P. J. (1994). The role of hydrological processes in ocean-atmosphere interactions. *Reviews of Geophysics*, *32*(4), 427–476. https://doi.org/10.1029/94RG01873

Webster, P. J., Magana, V. O., Palmer, T. N., Shukla, J., Tomas, R. A., Yanai, M. U., & Yasunari, T. (1998). Monsoons: Processes, predictability, and the prospects for prediction. *Journal of Geophysical Research*, *103*(C7), 14451–14510. https://doi.org/10.1029/97JC02719

Wei, G., Li, X. H., Liu, Y., Shao, L., & Liang, X. (2006). Geochemical record of chemical weathering and monsoon climate change since the early Miocene in the South China Sea. *Paleoceanography*, *21*(4). https://doi.org/10.1029/2006PA001300

Wei, G., Liu, Y., Ma, J., Xie, L., Chen, J., Deng, W., & Tang, S. (2012). Nd, Sr isotopes and elemental geochemistry of surface sediments from the South China sea: Implications for provenance tracing. *Marine Geolology.*, *319*, 21–34. https://doi.org/10.1016/j.margeo.2012.05.007

Wu, M. C. (1992). On the monitoring and prediction of the summer drought in Taiwan area (I): Meteorological conditions in the abundant and deficit rainfall years. *Atmospheric Science*, *20*, 35–46. In Chinese.

Wu, Q. (2014). New insights into the current- and past hydrology of the north-western subtropical Pacific Ocean over the past 25 kyr, based on investigations of the Nd isotopic composition of seawater and deep-sea sediments from the northern South China Sea. Geochemistry. Université Paris Sud - Paris XI.

Xia, X. M., Li, Y., Yang, H., Wu, C. Y., Sing, T. H., & Pong, H. K. (2004). Observations on the size and settling velocity distributions of suspended sediment in the Pearl River Estuary, China. *Continental Shelf Research*, *24*(16), 1809–1826. https://doi.org/10.1016/j.csr.2004.06.009

Xie, L., Tian, J., Zhang, S., Zhang, Y., & Yang, Q. (2011). An anticyclonic eddy in the intermediate layer of the Luzon Strait in Autumn 2005. *Journal of Oceanography*, *67*(1), 37–46. https://doi.org/10.1007/s10872-011-0004-9

Xu, Y., Wang, S., Bai, X., Shu, D., & Tian, Y. (2018). Runoff response to climate change and human activities in a typical karst watershed, SW China. *PLoS One*, *13*(3), e0193073. https://doi.org/10.1371/journal.pone.0193073

Xue, Y., Ji, J., Sun, S., Wu, G., Lau, K. M., Poccard, I., et al. (2005). Multiscale variability of the river runoff system in China and its long-term link to precipitation and sea surface temperature. *Journal of Hydrometeorology*, *6*(4), 550–570. https://doi.org/10.1175/JHM439.1

Yancheva, G., Nowaczyk, N. R., Mingram, J., Dulski, P., Schettler, G., Negendank, J., et al. (2007). Influence of the intertropical convergence zone on the East Asian monsoon. *Nature*, *445*(7123), 74–77. https://doi.org/10.1038/nature05431

Yang, Q., Tian, J., & Zhao, W. (2010). Observation of Luzon Strait transport in summer 2007. *Deep-Sea Research Part I*, *57*(5), 670–676. https://doi.org/10.1016/j.dsr.2010.02.004

Yu, S. W., Tsai, L. L., Talling, P. J., Lin, A. T., Mii, H. S., Chung, S. H., & Horng, C. S. (2017). Sea level and climatic controls on turbidite occurrence for the past 26 kyr on the flank of the Gaoping Canyon off SW Taiwan. *Marine Geology*, *392*, 140–150. https://doi.org/10.1016/j.margeo.2017.08.011

Yu, Z., Wan, S., Colin, C., Yan, H., Bonneau, L., Liu, Z., et al. (2016). Co-evolution of monsoonal precipitation in East Asia and the tropical Pacific ENSO system since 2.36 Ma: New insights from high-resolution clay mineral records in the West Philippine Sea. *Earth and Planetary Science Letters*, *446*, 45–55. https://doi.org/10.1016/j.epsl.2016.04.022

Yuan, D. (2002). A numerical study of the South China Sea deep circulation and its relation to the Luzon Strait transport. *Acta Oceanologica Sinica*(2), 187–202.

Zhang, W., Wei, X., Jinhai, Z., Yuliang, Z., & Zhang, Y. (2012). Estimating suspended sediment loads in the Pearl River Delta region using sediment rating curves. *Continental Shelf Research*, *38*, 35–46. https://doi.org/10.1016/j.csr.2012.02.017

Zhang, W., Yan, H., Dodson, J., Cheng, P., Liu, C., Li, J., et al. (2018). The 9.2 ka event in Asian summer monsoon area: The strongest millennial scale collapse of the monsoon during the Holocene. *Climate Dynamics*, *50*(7–8), 2767–2782. https://doi.org/10.1007/s00382-017-3770-2

Zhang, Y., Liu, Z., Zhao, Y., Colin, C., Zhang, X., Wang, M., et al. (2018). Long-term in situ observations on typhoon-triggered turbidity currents in the deep sea. *Geology*, *46*(8), 675–678. https://doi.org/10.1130/G45178.1

Zhao, S., Liu, Z., Colin, C., Zhao, Y., Wang, X., & Jian, Z. (2018). Responses of the East Asian summer monsoon in the low-latitude South China Sea to high-latitude millennial-scale climatic changes during the last glaciation: Evidence from a high-resolution clay mineralogical record. *Paleoceanography and Paleoclimatology*, *33*(7), 745–765. https://doi.org/10.1029/2017PA003235

Zhao, Y., Liu, Z., Zhang, Y., Li, J., Wang, M., Wang, W., & Xu, J. (2015). In situ observation of contour currents in the northern South China Sea: Applications for deepwater sediment transport. *Earth and Planetary Science Letters*, *430*, 477–485. https://doi.org/10.1016/j.epsl.2015.09.008

Zhao, Y., Yang, S., Liu, J. T., Fan, D., Yang, R. J., Bi, L., & Chang, Y. P. (2017). Reconstruction of silicate weathering intensity and paleoenvironmental change during the late Quaternary in the Zhuoshui River catchment in Taiwan. *Quaternary International*, *452*, 43–53. https://doi.org/10.1016/j.quaint.2016.12.013

Zhou, L., Gao, S., Jia, J., Yang, Y., Tong, C., & Wang, A. (2021). Paleo-typhoon events as indicated by coral Reef Boulder deposits on the southern coast of Hainan island, China. *Frontiers in Marine Science*, *8*, 746773. https://doi.org/10.3389/fmars.2021.746773

Zhou, L., Yang, Y., Wang, Z., Jia, J., Mao, L., Li, Z., et al. (2019). Investigating ENSO and WPWP modulated typhoon variability in the South China Sea during the mid–late Holocene using sedimentological evidence from southeastern Hainan Island, China. *Marine Geology*, *416*, 105987. https://doi.org/10.1016/j.margeo.2019.105987

Zhou, X., Sun, L., Zhan, T., Huang, W., Zhou, X., Hao, Q., et al. (2016). Timetransgressive onset of the Holocene optimum in the East Asian monsoon region. *Earth and Planetary Science Letters*, *456*, 39–46. https://doi.org/10.1016/j.epsl.2016.09.052

Zhu, Y., Sun, J., Wang, Y., Li, S., Xu, T., Wei, Z., & Qu, T. (2019). Overview of the multi-layer circulation in the South China sea. *Progress in Oceanography*, *175*, 171–182. https://doi.org/10.1016/j.pocean.2019.04.001

References From the Supporting Information

Andersen, K.-K., Azuma, N., Barnola, J.-M., Bigler, M., Biscaye, P., Caillon, N., & Chappellaz, J. (2004). High-resolution record of Northern Hemisphere climate extending into the last interglacial period. *Nature*, *431*(7005), 147–151. https://doi.org/10.1038/nature02805

Lisiecki, L. E., & Raymo, M. E. (2005). A Pliocene-Pleistocene stack of 57 globally distributed benthic δ18O records. *Paleoceanography*, *20*(1). https://doi.org/10.1029/2004PA001071